Engineering Geology 293 (2021) 106323

Contents lists available at ScienceDirect

Engineering Geology

journal homepage: www.elsevier.com/locate/enggeo

Coseismic vertical ground deformations vs. intensity measures: Examples from the Apennines

Omar Al Shawa [a], Simone Atzori [b], Carlo Doglioni [c,b,*], Domenico Liberatore [a], Luigi Sorrentino [a], Andrea Tertulliani [b]

[a] Department of Structural and Geotechnical Engineering, Sapienza University, Rome, Italy
[b] Istituto Nazionale di Geofisica e Vulcanologia, Rome, Italy
[c] Department of Earth Sciences, Sapienza University, Rome, Italy

ARTICLE INFO

Keywords:
Earthquakes epicentral area
Coseismic vertical shaking
DInSAR data
Macroseismic intensity
Ground motion intensity measures

ABSTRACT

DInSAR data provide a powerful tool to recognize the Earth's surface where permanent deformations are concentrated and undergo the strongest ground motion during an earthquake, i.e., defining the epicentral area. We analyzed three recent seismic events in the Apennines belt in Italy related to extensional and contractional earthquakes and documented that the largest macroseismic intensity is recorded where the ground underwent the largest vertical component of motion and the stronger vertical component of the peak ground acceleration. Besides site amplification effects that may occur everywhere even outside the epicentral area, we infer that the vertical oscillations in the so-called near-field allow the horizontal shaking to be more effective, hence producing larger damage above the active crustal volume. The active volume is the one moving vertically and is contemporaneously crossed by seismic waves nucleated by the shear on the fault. The surrounding passive volume in the far field is only crossed by seismic waves. The near field areas are elliptical and cover areas of 300–600 km^2 for a range of M_w 6–6.9, and they should be the areas where the highest seismic hazard must be expected. Therefore, their area is too large to be neglected for seismic hazard assessment.

1. Introduction

The Differential Synthetic Aperture Radar interferometry (DInSAR) data provide a powerful tool to analyze ground deformations occurring during an earthquake (Massonnet et al., 1993; Salvi et al., 2000; Pedersen et al., 2003; Hernandez et al., 2004; Akoglu et al., 2006; Wang et al., 2007; Li et al., 2008; Atzori et al., 2009; Belabbès et al., 2009; Weston et al., 2012; Wang et al., 2014; Kuang et al., 2019; Monterroso et al., 2020; Valerio et al., 2020). The images of the ground deformation are the fingerprint of the volume affected by strain in the hanging wall of dip-slip faults such as thrusts or normal faults (Petricca et al., 2021). Contractional and extensional earthquakes represent the dissipation of elastic and gravitational energy, respectively (Doglioni et al., 2015; Bignami et al., 2020; Albano et al., 2021a,b) and the strain is mostly concentrated in the mobilized hanging wall volume where the energy was stored during the interseismic period and where the deformation is maximum at coseismic stage (Petricca et al., 2021). In fact, the largest number of surface landslides and surface effects are concentrated in the same hanging wall area (Martino et al., 2014). Footwall deformation and shaking are far lower than in the hanging wall (Tizzani et al., 2013; Valerio et al., 2018; Bignami et al., 2019; Petricca et al., 2021) It was also demonstrated that the area where the vertical component of shaking is the highest the damage to masonry buildings with poor mechanical characteristics is greater due to their consequent strength weakening (Liberatore et al., 2019). In this article we compare the vertical component of punctual displacements of the ground recorded by DInSAR that allow reconstructing the areal ground deformation with the macroseismic intensity distribution and with ground motion intensity measures. This provides further evidence of the importance of the vertical shaking in controlling the disruption of the buildings, which is concentrated in the epicentral area recorded throughout the DInSAR images. For this purpose, we present the ri-elaboration of the satellite data of the three major seismic sequences in the Apennines of the last twelve years, i.e., the normal fault-related M_w 6.3 L'Aquila 2009, the thrust-related M_w 6 and M_w 5.9 Emilia 2012, and the normal fault-related M_w 6 and 6.5 Amatrice-Norcia 2016 earthquakes, integrating

* Corresponding author at: Department of Earth Sciences, Sapienza University, Rome, Italy.
E-mail address: carlo.doglioni@uniroma1.it (C. Doglioni).

https://doi.org/10.1016/j.enggeo.2021.106323
Received 3 March 2021; Received in revised form 26 July 2021; Accepted 6 August 2021
Available online 10 August 2021

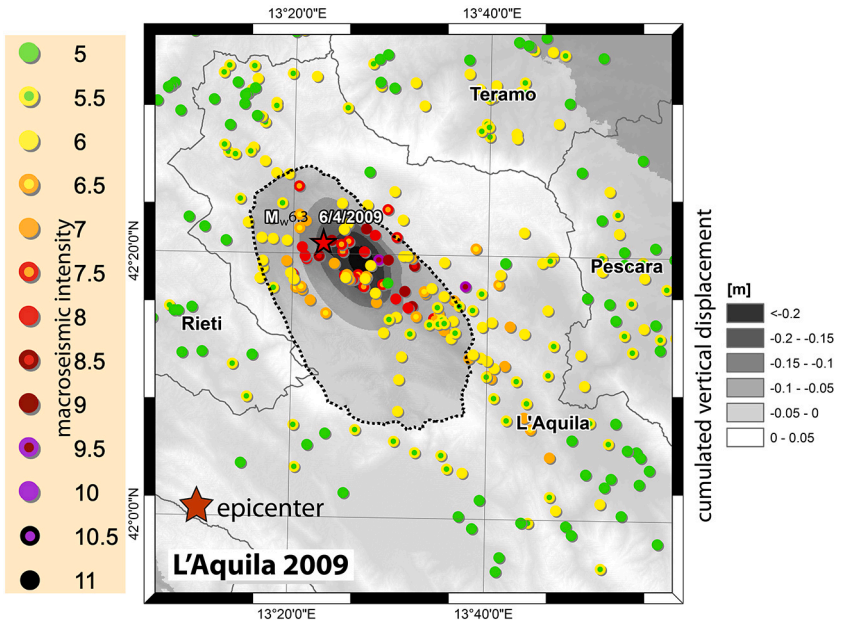

Fig. 1. Coseismic subsidence computed through DInSAR data compared to the macroseismic intensity of the M_w 6.3 April 6th 2009 L'Aquila Earthquake. Most of the damage occurred in the area that underwent vertical deformation, apart from rare scattered local amplification sites outside the elliptic area.

the ground deformation with the macroseismic intensity and ground motion intensity measures.

2. Geological setting

The Apennines are an arcuate fold and thrust belt followed by an extensional backarc wave in the hanging wall of a west-directed subduction, where the Adriatic and Ionian lithosphere sink westward and retreat relatively eastward (Doglioni, 1991). Italian tectonics is very active in the order of 2–5 mm/yr detected by space geodesy data (Devoti et al., 2008, 2017), and generating a diffuse seismicity (Chiarabba et al., 2005). The rocks involved in the accretionary prism are mainly 4–6 km thick passive margin sequences buried by 2–8 km thick active margin foredeep sediments such as flysch and molasse (Carminati and Doglioni, 2012). These thick foredeep deposits and deep foreland basins are typical of west-directed subduction zones where more than 1 mm/yr subsidence occurs (Doglioni, 1994). This is the reason why the Apennines have extensive, widespread, and thick flysch deposits pertaining to the foredeep basin developed since at least the Oligocene to present. The depocenter of the foredeep basin or piggy-back basins formed on top of the accretionary prism migrated from west to east, up to the present southern margin of the Po Basin, and all along the western margin of the Adriatic Sea. The remnants of the past foredeep deposits are now widespread along the mountain range. The Apennines migrated easterly contemporaneously with the slab retreat in the same direction at a speed (>4 mm/yr) faster than the erosion rate (<1 mm/yr) determining the highest peaks misplaced eastward relative to the water divide that is trying to keep track of the tectonic motion (Salustri Galli et al., 2002; Carminati and Doglioni, 2012). Active tectonics and the occurrence of low-friction flysch foredeep deposits determine diffuse geomorphological instabilities that register more than 600.000 landslides in Italy (ISPRA, 2007; Trigila and Iadanza, 2008) which are activated mostly by meteorological extreme rainflow (Brunetti et al., 2010), but also by seismicity (Del Gaudio and Wasowski, 2004; Vanmaercke et al., 2017).

3. Vertical ground deformation maps

The vertical component of the permanent ground deformation maps after L'Aquila (2009), Emilia (2012) and Amatrice-Norcia (2016) earthquakes is based on the source model derived from DInSAR data. They are 1-D displacement measurements obtained from the phase difference of two radar images acquired before and after the earthquake (Massonnet et al., 1993). Measurements are made along the Line-of-Sight (LoS), a vector connecting the satellite to the pixel on the ground and positive toward the satellite. The LoS vector has an angle of 20÷40 degrees from the vertical direction and an azimuth angle close to, but not perfectly coincident with, the East-West direction. Because of this peculiar geometry, orthogonal to none of the Cartesian axes, the LoS is a composition of fractions of W-E, N-S and vertical displacement components. Therefore, inferring a single component, as the vertical one, straight from DInSAR measurement is mathematically undetermined (one equation and three unknowns). It often occurs that two different LoS are available, from ascending and descending orbits; though they can be combined, the problem is still undetermined (two equations and three unknowns). Hence, a third condition can be introduced, assuming that the North-South displacement component is null, being nearly orthogonal to the LoS. This assumption, however, introduces approximations that under some circumstances are not negligible. We, therefore, adopt a model-based approach; this approach exploits the nowadays consolidated process to infer the seismic source from DInSAR data (Wright et al., 2003; Biggs and Wright, 2020). The combination of reliable analytical models and optimization algorithms allows retrieving the source best predicting the observed DInSAR data, through inverse data modelling. We then use the seismic source model to generate the ground deformation maps in the E-W, N-S and vertical direction (forward modelling), without introducing any approximation or assumption on the N-S deformation component. This model-based approach to get a complete 3D ground deformation has the further advantage of filtering out most of the atmospheric artefacts that generally affect DInSAR maps; while they cannot be a priori discriminated from the real displacement signal, they are absent in the forward calculation (Liberatore et al., 2019).

For these three events, we exploit refined sources obtained from the inversion of DInSAR data obtained pairing images from the satellites/constellations Envisat, COSMO-SkyMed, ALOS-Palsar and Sentinel-1, already presented in a number of publications (Atzori et al., 2009; Lanari et al., 2010; Stramondo et al., 2010; Trasatti et al., 2011; Guglielmino et al., 2013; Pezzo et al., 2013; Lavecchia et al., 2016;

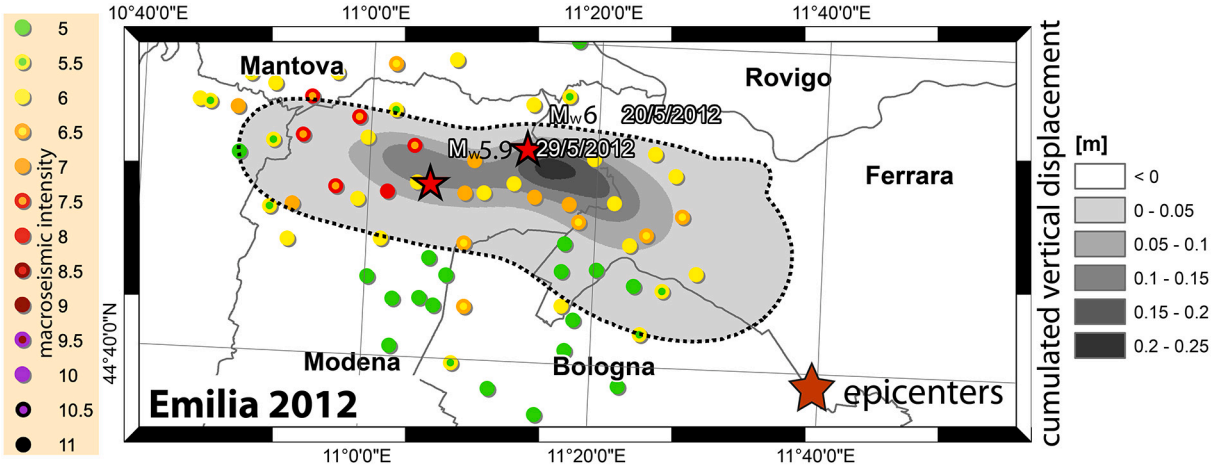

Fig. 2. Coseismic uplift computed through DInSAR data compared to the macroseismic intensity of the M_w 6 and 5.9 Emilia May 20th and 29th 2012 Emilia seismic sequence. Most of the damage occurred in the area that underwent vertical deformation, apart from rare scattered local amplification sites and liquefaction outside the elliptic area.

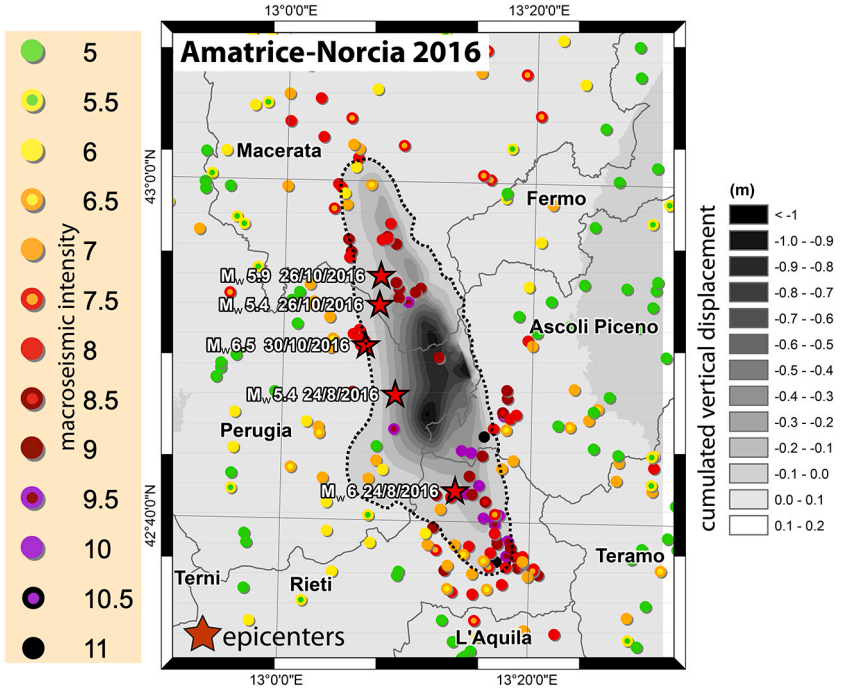

Fig. 3. Coseismic subsidence computed through DInSAR data compared to the macroseismic intensity of the M_w 6 and 6.5 Amatrice-Norcia August 24th and October 30th 2016 Central Italy seismic sequence. Most of the damage occurred in the area that underwent vertical deformation, apart from rare scattered local amplification sites outside the elliptic area.

Cheloni et al., 2017). The vertical ground deformation maps obtained for the three earthquakes with this model-based approach are shown in Figs. 1–3.

4. Macroseismic data

Macroseismic intensity is a tool to evaluate the effect of the ground motion, collecting data on the building damage based on a classification described by the macroseismic scales. Nowadays in Italy the most used macroseismic scale during post-earthquakes field surveys is the European Macroseismic Scale - 98 (EMS-98, Grünthal, 1998), which allows to classify the buildings for their vulnerability and the grades of damage they suffered. Until about twenty years ago, and more recently in some cases, the Mercalli-Cancani-Sieberg (MCS) scale was commonly used for the same purpose. Even if the macroseismic intensity is a discrete measure, it is the best detector of the earthquake's effects on the human environment, as it can provide networks of observation points denser than any operating instrumental network.

4.1. M_w 6.3 L'Aquila April 6th 2009

In this approach we used a macroseismic intensity dataset of the L'Aquila 2009 earthquake (Galli et al., 2009) consisting of 315 localities, 130 of them with an intensity greater than VI MCS. Six localities suffered effects of intensity equal to or larger than IX MCS (Fig. 1). Maximum intensities were recorded in the villages of Onna and Castelnuovo (IX-X MCS), whose high intensities were due to a site effect (Evangelista et al., 2016; Mele et al., 2020). We have to underline that the village of

Table 1
MCS intensities and DInSAR vertical displacements for L'Aquila earthquake ($I_{MCS} \geq$ VII).

Site	Municipality and province abbreviation	I_{MCS}	w (m)
Onna	L'Aquila AQ	IX-X	−0.1677
Castelnuovo	San Pio delle Camere AQ	IX-X	0.0028
San Gregorio	L'Aquila AQ	IX	−0.1111
Tempera	L'Aquila AQ	IX	−0.0761
Sant'Eusanio Forconese	Sant'Eusanio Forconese AQ	IX	−0.0441
Villa Sant'Angelo	Villa Sant'Angelo AQ	IX	−0.0306
L'Aquila	L'Aquila AQ	VIII-IX	−0.1442
Poggio di Roio	L'Aquila AQ	VIII-IX	−0.1030
Poggio Picenze	Poggio Picenze AQ	VIII-IX	−0.0104
Bazzano	L'Aquila AQ	VIII	−0.2141
Casentino	Sant'Eusanio Forconese AQ	VIII	−0.0743
Paganica	L'Aquila AQ	VIII	−0.0639
Roio Piano	L'Aquila AQ	VIII	−0.0634
Santa Rufina	L'Aquila AQ	VIII	−0.0601
Colle di Roio	L'Aquila AQ	VIII	−0.0581
Tussillo	Villa Sant'Angelo AQ	VIII	−0.0390
Civita di Bagno	L'Aquila AQ	VII-VIII	−0.1997
Sant'Elia	L'Aquila AQ	VII-VIII	−0.1805
San Benedetto di Bagno	L'Aquila AQ	VII-VIII	−0.1786
Gignano	L'Aquila AQ	VII-VIII	−0.1783
Torretta	L'Aquila AQ	VII-VIII	−0.1711
Sant'Angelo di Bagno	L'Aquila AQ	VII-VIII	−0.1690
San Felice d'Ocre	Ocre AQ	VII-VIII	−0.1667
Bagno Grande	L'Aquila AQ	VII-VIII	−0.1579
Fossa	Fossa AQ	VII-VIII	−0.1470
Colle di Lucoli	Lucoli AQ	VII-VIII	−0.0241
Fagnano Alto (Vallecupa)	Fagnano Alto AQ	VII-VIII	−0.0094
Arischia	L'Aquila AQ	VII-VIII	−0.0074
Pescomaggiore	L'Aquila AQ	VII-VIII	0.0003
Camarda	L'Aquila AQ	VII-VIII	0.0164
Bagno Piccolo	L'Aquila AQ	VII	−0.1670
Vallesindola di Bagno	L'Aquila AQ	VII	−0.1612
Pianola	L'Aquila AQ	VII	−0.1449
San Martino d'Ocre	Ocre AQ	VII	−0.1119
Pettino	L'Aquila AQ	VII	−0.0572
Prato Lonaro	Lucoli AQ	VII	−0.0292
Collefracido	L'Aquila AQ	VII	−0.0215
Collarano	San Demetrio ne' Vestini AQ	VII	−0.0109
Corbellino	Fagnano Alto AQ	VII	−0.0085
Pedicciano	Fagnano Alto AQ	VII	−0.0046
Tione degli Abruzzi	Tione degli Abruzzi AQ	VII	0.0003
Goriano Sicoli	Goriano Sicoli AQ	VII	0.0011
Roccapreturo	Acciano AQ	VII	0.0013
Castelvecchio Subequo	Castelvecchio Subequo AQ	VII	0.0013
Civitaretenga	Navelli AQ	VII	0.0017

AQ: L'Aquila.

Castelnuovo is located just outside the epicentral area defined by the DInSAR (Fig. 1). In the earthquake area coexist very different building typologies, such as old centres, characterized by a traditional poor masonry, together with new expansion areas with reinforced concrete (hereinafter RC) recent buildings. Local unreinforced masonry buildings, highly vulnerable, suffered the greater amount of damage. Most of the severely damaged villages (i.e., higher intensities) were settled along the Medium Aterno Valley, SE of L'Aquila, and concentrated in the hanging wall of the Paganica-San Demetrio fault systems (Galli et al., 2009).

4.2. M_w 6 and 5.9 Emilia May 20th and 29th 2012

The maximum intensity EMS-98 of the Emilia 2012 seismic sequence was VIII and it represents the cumulative value (Fig. 2) due to the two main shocks of May 20th and 29th 2012 (Tertulliani et al., 2012). The sequence impacted an area where the most common building typologies are old traditional brick masonry houses and recent residential buildings in brick masonry or reinforced concrete. Old traditional brick masonry houses in the historical centers, and in the countryside, are often lacking connections or strengthening elements like tie rods or buttresses. In these cases the vulnerability classes, A or B according to EMS-98, were assigned depending on the state of maintenance. Strengthening elements, commonly found in other Italian areas prone to significant seismic activity, seemed not to belong to the building tradition of the Po Valley, even for historical mansions. Recent one-or-two-stories residential dwellings, in brick masonry or RC, are mainly sited in the outskirts of villages and towns (vulnerability classes B and C), and nowadays are more common than the traditional brick masonry buildings. In this seismic sequence this recent residential building stock did not suffer much damage, and this is the reason why the intensity values are quite limited. A greater damage, total or near total collapses, hit special and monumental buildings: industrial warehouses, farmhouses, barns, churches, towers or belfries, statistically not significant in the intensity assessment. A rough observation of the macroseismic dataset (Fig. 2) shows a clustering of the highest intensities to the western part of the epicentral area of the May 29th shock, probably due to cumulative effects after the second earthquake.

4.3. M_w 6 and 6.5 Amatrice-Norcia August 24th and October 30th 2016

The macroseismic data, in terms of the EMS-98, have been collected during several field surveys that were performed following each one of the main earthquakes of the seismic sequence, from August 2016 to January 2017 (Azzaro et al., 2016; Rossi et al., 2019). It is recognized that during a seismic sequence, buildings that suffer repeated shocks in a limited span of time, undergo a progressive deterioration of their strength characteristics (i.e., Grimaz and Malisan, 2017; Mouyiannou et al., 2014). The related increase of the building vulnerability and the progressive aggravation of the damage are not evaluable in terms of intensity scales (Rossi et al., 2019). For this reason, from a macroseismic point of view, it is very difficult to assess the contribution of single aftershocks: it is hence inevitable to assess a cumulative intensity that considers the final observed damage provoked by the whole sequence (Graziani et al., 2017; Graziani et al., 2019). The already devastating picture caused by the M_w 6 August 24th 2016 earthquake in the Amatrice area, was escalated and made wider by the October 26th and 30th, 2016 earthquakes. Macroseismic cumulated intensity assessed for the 2016–2017 sequence (Fig. 3) reached intensity XI EMS-98 in Amatrice and Pescara del Tronto, and intensity X EMS-98 in several other sites. Fiorentino et al. (2018) acknowledged that one of the main causes of such destruction consisted in the high vulnerability of the traditional building stock, manufactured by simple stones, irregular in size and assembled with a poor quality of mortar (see also Rossi et al., 2019), as well as site amplification in the Amatrice terrace (Milana et al., 2019).

5. Relations between DInSAR vertical ground deformation vs. macroseismic intensity

A group of empirical relations between DInSAR vertical component of the ground deformation recorded by single displacement points and macroseismic intensity was then investigated for the L'Aquila earthquake (mainshock on April 6th, 2009, M_w 6.3), Emilia 2012 earthquake (second shock on May 29th, 2012, M_w 5.9) and Amatrice-Norcia earthquakes (shock on August 24th, 2016, M_w 6.0). Concerning the

Table 2
MCS intensities, EMS-98 intensities and DInSAR vertical displacements for Amatrice earthquake, August 24th, 2016 ($I_{MCS} \geq$ VII or $I_{EMS} \geq$ VII).

Site	Municipality and province abbreviation	I_{MCS}	I_{EMS}	w (m)
Amatrice	Amatrice RI	X-XI	X	−0.0464
Petrana	Amatrice RI	X-XI	IX-X	−0.0819
Pescara del Tronto	Arquata del Tronto AP	X-XI	X	−0.0764
Illica	Accumoli RI	X	IX-X	−0.1984
Casale	Amatrice RI	X	IX-X	−0.0948
Saletta	Amatrice RI	X	X	−0.1492
Rio	Amatrice RI	IX-X		−0.0870
San Lorenzo e Flaviano	Amatrice RI	IX-X	IX-X	−0.0947
Sant'Angelo	Amatrice RI	IX-X	IX-X	−0.0468
Faizzone	Amatrice RI	IX		−0.0635
Sommati	Amatrice RI	IX	IX	−0.0301
Crognale	Amatrice RI		IX	−0.0790
Accumoli	Accumoli RI	VIII-IX	VIII	−0.1740
Grisciano	Accumoli RI	VIII-IX	VIII-IX	−0.0953
Poggio Casoli	Accumoli RI	VIII-IX	VIII-IX	−0.1651
Cornillo Vecchio	Amatrice RI	VIII-IX	VIII	−0.0689
Cossito	Amatrice RI	VIII-IX	VIII	−0.0564
Retrosi	Amatrice RI	VIII-IX	VIII	−0.0175
Rocchetta	Amatrice RI	VIII-IX	VIII	−0.0959
Arquata del Tronto	Arquata del Tronto AP	VIII-IX	VIII-IX	0.0027
Capodacqua	Arquata del Tronto AP	VIII-IX	VIII-IX	−0.1672
Tufo	Arquata del Tronto AP	VIII-IX	VIII-IX	−0.1557
Fonte del Campo	Accumoli RI	VIII	VII-VIII	−0.2148
Cascello	Amatrice RI	VIII	VII-VIII	−0.0325
Moletano	Amatrice RI	VIII	VIII	−0.0155
Santo Masso	Amatrice RI	VIII		−0.0930
San Giovanni	Accumoli RI	VII-VIII	VIII	−0.0388
Tino	Accumoli RI	VII-VIII	VII-VIII	−0.2043
Collepagliuca	Amatrice RI	VII-VIII	VII-VIII	−0.0254
Prato	Amatrice RI	VII-VIII	VIII-IX	−0.0478
San Capone	Amatrice RI	VII-VIII		−0.0777
Pretare	Arquata del Tronto AP	VII-VIII	VII-VIII	0.0037
Cossara	Amatrice RI		VII-VIII	−0.0144
Fornisco	Valle Castellana TE		VII-VIII	0.0017
Villanova	Accumoli RI	VII	VI-VII	−0.0865
Capricchia	Amatrice RI	VII	VII	0.0090
Poggio Vitellino	Amatrice RI	VII		−0.0964
San Lorenzo a Pinaco	Amatrice RI	VII		−0.0081
Scai	Amatrice RI	VII	VII	0.0050
Torrita	Amatrice RI	VII		0.0031
Voceto	Amatrice RI	VII	VIII	0.0012
Borgo	Arquata del Tronto AP	VII	VII	0.0015
Faete	Arquata del Tronto AP	VII		0.0088
Piedilama	Arquata del Tronto AP	VII	VII	0.0041
Trisungo	Arquata del Tronto AP	VII	VII	0.0106
Castro	Montegallo AP	VII	VII	0.0042
San Pellegrino	Norcia PG	VII	VII-VIII	−0.0213
Faete	Arquata del Tronto AP		VII	0.0087
Poggio d'Api	Accumoli RI		VII	0.0054
Santa Lucia	Montereale AQ		VII	0.0043
Tallacano	Acquasanta Terme AP		VII	0.0049
Vezzano	Arquata del Tronto AP		VII	−0.0109
Arafranco-Pinaco	Amatrice RI	VI-VII	VII	−0.0039
Castel Trione	Amatrice RI	VI-VII	VII-VIII	0.0082
Cornelle di Sotto	Amatrice RI	VI-VII	VII-VIII	0.0019
Ferrazza	Amatrice RI	VI-VII	VII-VIII	−0.0045
Preta	Amatrice RI	VI-VII	VII	0.0080
San Cipriano	Amatrice RI	VI-VII	VII	−0.0182
Gualdo	Castelsantangelo sul Nera MC	VI	VII	−0.0047

AP: Ascoli Piceno, AQ: L'Aquila, MC: Macerata, PG: Perugia, RI: Rieti, TE: Teramo.

latter, although DInSAR recorded deformation was somewhere higher in the following events, like that on October 30th, 2016, the determination of these relations is more problematic because of cumulated intensity. In fact, the cumulated ground deformation of a sequence of events is additive (it is the sum of the deformation of the individual events), whereas cumulated intensity is not. In fact, ground deformation cumulates as a consequence of multiple mainshocks, whereas the macroseismic intensity of a seismic sequence is not just the sum of the intensities of the individual events, and the macroseismic intensity of localities that were already highly damaged by the first mainshock cannot be simply added up because the second event acted on highly weakened or already partly collapsed buildings (see Grimaz and Malisan, 2017; Graziani et al., 2019).

The MCS intensities I_{MCS} for L'Aquila 2009 (Galli et al., 2009), the MCS and EMS-98 intensities for Central Italy Amatrice-Norcia 2016 (Galli et al., 2016; Azzaro et al., 2016) earthquakes, respectively, along with the corresponding modelled DInSAR vertical displacements, denoted by w, are reported in Figs. 1 and 3 and in Tables 1 and 2. The assignment of intensity degree was performed by counting the number of damaged or collapsed buildings in comparison with the total building number.

The EMS-98 intensities I_{EMS} for Emilia 2012 compressive earthquake (Tertulliani et al., 2012) are reported in Fig. 2 and in Table 3, along with the corresponding modelled DInSAR vertical displacements. These intensities cumulate the effects of the shocks on May 20th, M_w 6.0, and on May 29th, M_w 5.9 (Rovida et al., 2019). Besides counting the number of damaged/collapsed buildings, the EMS-98 intensity accounts for the different vulnerability classes of buildings.

L'Aquila 2009 and Amatrice-Norcia 2016 Central Italy earthquakes are characterized by a normal mechanism with downward DInSAR ground deformation in the epicentral zone of about 20 cm (Atzori et al., 2009) and 100 cm (Bignami et al., 2019), respectively, whereas the Emilia earthquake by a reverse mechanism with upward deformation of about 15 cm (Tizzani et al., 2013). The coseismic upward and downward

Table 3
EMS-98 intensities and DInSAR vertical displacements for the Emilia earthquake ($I_{EMS} \geq$ VII).

Site	Municipality and province abbreviation	I_{EMS}	w (m)
Cavezzo	Cavezzo MO	VIII	0.0478
Mirandola	Mirandola MO	VII-VIII	0.0996
Novi di Modena	Novi di Modena MO	VII-VIII	0.0207
Rovereto sulla Secchia	Novi di Modena MO	VII-VIII	0.0186
Concordia sulla Secchia	Concordia sulla Secchia MO	VII-VIII	0.0109
Moglia	Moglia MN	VIII	−0.0012
Finale Emilia	Finale Emilia MO	VII	0.1075
Ponte San Pellegrino	Mirandola MO	VII	0.0964
Canaletto	Finale Emilia MO	VII	0.0922
San Felice sul Panaro	San Felice sul Panaro MO	VII	0.0889
Fossoli	Carpi MO	VII	0.0013
Reggiolo	Reggiolo RE	VII	−0.0014

MN: Mantova, MO: Modena, RE: Reggio Emilia.

Table 4
Regressions of DInSAR displacement (w) and macroseismic intensity (I_{MCS} or I_{EMS}).

		a	b	SE(a)	SE(b)	SE(y)	n	R^2	α_F	α_{LR}
L'Aquila, 2009, V $\leq I_{MCS} \leq$ IX-X	w - I_{MCS}	−0.02736 m	0.14262 m	0.00241 m	0.01422 m	0.03934 m	307	0.2977	3.30 10^{-25}	2.12 10^{-25}
	I_{MCS} - w	−10.878 m^{-1}	5.6476	0.9568 m^{-1}	0.04762	0.7843				
Amatrice-Norcia, 2016, V $\leq I_{MCS} \leq$ X-XI	w - I_{MCS}	−0.02152 m	0.11329 m	0.00182 m	0.01138 m	0.03408 m	165	0.4631	8.87 10^{-24}	4.08 10^{-24}
	I_{MCS} - w	−21.521 m^{-1}	5.7135	1.8152 m^{-1}	0.0900	1.0777				
Emilia, 2012, V $\leq I_{EMS} \leq$ VIII	w - I_{EMS}	0.02104 m	−0.10367 m	0.00531 m	0.03156 m	0.03587 m	70	0.1874	1.82 10^{-4}	1.38 10^{-4}
	I_{EMS} - w	8.9067 m^{-1}	5.7063	2.2494 m^{-1}	0.0991	0.7381				

Table 5
Regressions of DInSAR displacement (w) and macroseismic intensity (I_{MCS}) for L'Aquila and Amatrice earthquake, V $\leq I_{MCS} \leq$ X-XI.

	a	b	SE(a)	SE(b)	SE(y)	n	R^2	α_F	α_{LR}
w - I_{MCS}	−0.02379 m	0.12364 m	0.00151 m	0.00910 m	0.03774 m	472	0.3465	2.39 10^{-45}	1.40 10^{-45}
I_{MCS} - w	−14.567 m^{-1}	5.6736	0.9227 m^{-1}	0.04587	0.9340				

deformation in the extensional and contractional earthquakes, respectively, are about 5 to 10 times smaller than the opposite vertical ground deformation. Therefore, we focus on the primary deformation where larger shaking is expected and measured (Liberatore et al., 2019; Petricca et al., 2021), i.e., coseismic subsidence in the hanging wall of normal faults and coseismic uplift in the hanging wall of thrusts.

It can be observed that downward displacement for the centre of Amatrice on August 24th is moderate (w = −0.04643 m) but EMS-98 intensity reaches its highest value (I_{EMS} = X on August 24th, I_{EMS} = XI cumulating the events on August 24th and October 30th). Topographic amplification related to crest morphology and the underlying gravels of the terrace producing site amplification (Milana et al., 2019) and severe damage induced by poor masonry quality (Sorrentino et al., 2019) are reasonable explanations. On the other hand, MCS intensities after the August 24th event for sites such as Tino and Fonte del Campo, both in the municipality of Accumoli, with the greatest downward displacement, were moderate, namely VII-VIII and VIII, respectively. Similarly, downward displacement for the site of Forche Canepine, in the municipality of Arquata del Tronto, was high (w = −0.1463 m) with low intensity (I_{MCS} = V). However, this site has few buildings, possibly resulting in a non-robust estimation of intensity.

The regressions of DInSAR vertical displacement vs. macroseismic intensity (w - I_{MCS} or w - I_{EMS}) can be written as:

$$y = a\,x + b \tag{1}$$

where $y = w$ (m), $x = I_{MCS}$ or I_{EMS}, and the coefficients a, b are reported in Table 4 for the three earthquakes, along with the standard errors (SE) on a, b, y, the number of sites analyzed n and the coefficient of determination R^2. The regressions are also reported in Fig. 7. The regressions were determined by considering macroseismic intensities greater than or equal to V and hold for the intensity range indicated in Table 4. The higher the intensity, the higher the absolute value of w. The earthquakes with normal mechanisms have lower dispersion, and higher determination coefficients, compared to those with reverse mechanisms.

The statistical significance of the regressions was investigated by means of the F-test. Given the regression sum of squares $SSreg$ and the residual sum of squares $SSres$, the test statistic is $(SSreg/n_1)/(SSreg/n_2)$, with $n_1 = 1$, $n_2 = n - 2$, and follows a F-distribution with n_1 and n_2

Table 6
Ground motion intensity measures and DInSAR vertical displacements for L'Aquila earthquake, April 6th, 2009 ($w \leq$ −0.010 m).

Station	Soil type	Epicentral distance (km)	Dir.	PGA (cm/s^2)	PGV (cm/s)	IV (cm/s)	I_A (cm/s)	I_F (cm/s$^{3/4}$)	I_H (cm)	w (m)
IT.AQA	E	5.0	H	439.57	32.20	46.82	193.97	52.38	101.81	−0.0380
			V	435.57	9.36	11.85	60.99	14.89	31.95	
IT.AQG	B	5.0	H	479.46	38.91	62.56	146.89	66.49	118.37	−0.0380
			V	234.71	10.40	13.29	31.63	17.61	32.43	
IT.AQK	B	1.8	H	380.17	45.36	72.98	141.41	80.28	183.72	−0.1466
			V	355.60	20.05	27.07	112.25	36.04	67.30	
IT.AQV	B	4.9	H	755.45	46.52	67.34	285.41	77.04	131.80	−0.0402
			V	486.85	12.41	21.26	90.87	19.44	41.74	
MN.AQU	B[a]	2.2	H	345.92	34.42	55.95	95.45	55.82	118.42	−0.1430
			V	306.55	21.18	12.28	40.15	36.09	55.13	

[a] Site classification is not based on a direct $V_{s,30}$ (average shear wave velocity in the top 30 m) measurement.

Table 7
Ground motion intensity measures and DInSAR vertical displacements for Amatrice-Norcia earthquake, October 30th, 2016 ($w \leq$ −0.010 m).

Station	Soil type	Epicentral distance (km)	Dir.	PGA (cm/s^2)	PGV (cm/s)	IV (cm/s)	I_A (cm/s)	I_F (cm/s$^{3/4}$)	I_H (cm)	w (m)
IT.CLO	A[a]	7.8	H	590.52	69.58	123.31	443.92	117.25	277.35	−0.7803
			V	782.34	68.64	75.33	471.99	118.62	163.20	
IT.CNE	C[a]	7.7	H	487.22	41.66	70.71	197.39	64.92	129.83	−0.1979
			V	536.70	24.92	22.03	216.04	44.56	64.51	
IT.FCC	A[a]	11.0	H	938.53	81.76	139.01	840.24	127.2	233.25	−0.4554
			V	923.42	44.62	65.56	433.57	68.67	155.70	
IV.T1213	A[a]	12.0	H	883.45	62.03	89.48	616.06	99.76	158.7	−0.0849
			V	869.24	32.54	28.96	291.46	49.88	90.52	
IV.T1214	B[a]	11.4	H	623.68	56.24	59.43	399.23	90.7	143.77	−0.4257
			V	633.16	30.50	38.40	149.45	47.74	109.47	

[a] Site classification is not based on a direct $V_{s,30}$ (average shear wave velocity in the top 30 m) measurement.

Table 8
Ground motion intensity measures and DInSAR vertical displacements for Emilia earthquake, May 29th, 2012 ($w \geq 0.010$ m).

Station	Soil type	Epicentral distance (km)	Dir.	*PGA* (cm/s^2)	*PGV* (cm/s)	*IV* (cm/s)	I_A (cm/s)	I_F (cm/s$^{3/4}$)	I_H (cm)	*w* (m)
BA.MIRE	C[a]	4.1	H	265.60	58.64	78.33	125.23	94.80	186.78	0.0978
			V	715.58	24.52	19.85	167.89	37.87	36.57	
BA.MIRH	C[a]	4.5	H	271.08	55.43	75.92	81.75	89.51	176.94	0.0985
			V	490.57	19.02	15.54	114.41	28.14	33.21	
IT.FIN0	C[a]	17.5	H	245.93	19.49	29.06	33.41	33.54	54.99	0.0971
			V	189.14	2.94	4.36	28.55	4.57	13.49	
IT.MRN	C	4.1	H	288.74	58.08	74.38	132.18	94.64	185.38	0.0978
			V	841.08	26.02	22.35	291.11	39.36	35.76	
IT.SAG0	C[a]	26.3	H	81.58	7.84	11.80	10.41	16.23	28.75	0.0540
			V	65.56	2.23	2.51	3.35	4.47	9.15	
IT.SAN0	C[a]	6.1	H	225.96	39.30	44.80	55.94	62.78	120.56	0.0856
			V	306.29	8.49	10.04	43.05	12.33	27.47	
IV.T0800	C[a]	14.4	H	330.74	28.10	54.88	99.15	44.39	91.79	0.1026
			V	313.97	4.83	7.35	22.84	7.39	12.11	
IV.T0802	C[a]	9.9	H	290.83	25.14	33.56	97.97	41.37	87.38	0.0883
			V	170.66	4.93	4.11	25.10	7.67	16.71	
IV.T0803	C[a]	24.0	H	123.08	9.20	14.65	15.18	16.79	35.22	0.0219
			V	66.23	1.96	2.45	3.40	3.57	5.93	
IV.T0805	C[a]	22.0	H	247.28	13.53	23.76	47.39	22.20	36.54	0.0185
			V	69.27	1.48	2.04	5.21	2.50	6.36	
IV.T0813	C[a]	11.3	H	368.14	29.61	39.07	126.43	46.10	81.73	0.0799
			V	171.22	3.81	4.32	17.65	5.95	11.32	
TV.CAS05	C[a]	33.0	H	83.87	6.86	10.01	8.08	14.66	29.59	0.0636
			V	46.20	1.57	3.12	2.56	3.77	9.79	
TV.MIR01	C[a]	0.5	H	432.78	53.28	91.84	193.37	86.53	214.67	0.0892
			V	361.68	13.72	14.12	86.19	21.09	41.68	
TV.MIR02	C[a]	5.1	H	281.20	57.48	69.80	128.88	93.03	172.97	0.0979
			V	452.46	11.99	11.22	109.53	18.52	33.68	
TV.MIR03	C[a]	11.2	H	335.64	34.39	59.41	136.30	56.00	114.69	0.0351
			V	398.45	6.82	8.98	87.75	10.95	23.03	
TV.MIR08	C[a]	8.6	H	248.58	32.45	54.27	114.14	51.90	142.49	0.0617
			V	306.80	7.82	10.40	54.16	12.41	28.43	
TV.MIR04	C[a]	13.0	H	418.09	36.33	69.19	148.67	55.64	146.95	0.0191
			V	258.36	5.71	5.58	38.02	9.10	19.63	
IT.BON0	C[a]	28.3	H	35.46	3.04	3.51	1.78	6.35	9.08	0.0173
			V	30.23	1.22	1.86	1.53	2.36	3.87	

[a] Site classification is not based on a direct $V_{s,30}$ (average shear wave velocity in the top 30 m) measurement.

Table 9
Regressions of intensity measures vs. *w*, L'Aquila, April 6th, 2009, $w \leq -0.010$ m, $n = 5$.

Direction		*a*	*b*	SE(*a*)	SE(*b*)	SE(*y*)	R^2	α_F	α_{LR}
Horizontal	*PGA*(*)	1802.50 cm/(m s^2)	626.418 cm/s^2	1232.663 cm/(m s^2)	118.80 cm/s^2	143.26 cm/s^2	0.4161	2.40 10^{-1}	1.01 10^{-1}
	PGV	−9.0421 cm/(m s)	38.748 cm/s	63.222 cm/(m s)	6.0933 cm/s	7.3475 cm/s	0.0068	8.95 10^{-1}	8.54 10^{-1}
	IV	−55.998 cm/(m s)	56.585 cm/s	95.595 cm/(m s)	9.2134 cm/s	11.111 cm/s	0.1026	5.99 10^{-1}	4.62 10^{-1}
	I_A (*)	832.60 cm/(m s)	240.20 cm/s	530.55 cm/(m s)	51.134 cm/s	61.659 cm/s	0.4508	2.15 10^{-1}	8.34 10^{-2}
	I_F	−31.040 cm/(m s$^{3/4}$)	63.883 cm/s$^{3/4}$	121.82 cm/(m s$^{3/4}$)	11.741 cm/s$^{3/4}$	14.158 cm/s$^{3/4}$	0.0212	8.15 10^{-1}	7.44 10^{-1}
	I_H	−329.07 cm/m	104.12 cm	247.75 cm/m	23.878 cm	28.793 cm	0.3703	2.76 10^{-1}	1.28 10^{-1}
Vertical	*PGA*(*)	491.75 cm/(m s^2)	403.77 cm/s^2	956.04 cm/(m s^2)	92.142 cm/s^2	111.11 cm/s^2	0.0810	6.42 10^{-1}	5.16 10^{-1}
	PGV	−93.317 cm/(m s)	7.1060 cm/s	11.378 cm/(m s)	1.0966 cm/s	1.3224 cm/s	0.9573	3.80 10^{-3}	7.16 10^{-5}
	IV	−42.576 cm/(m s)	13.694 cm/s	62.350 cm/(m s)	6.0092 cm/s	7.2462 cm/s	0.1345	5.44 10^{-1}	3.95 10^{-1}
	I_A	−156.22 cm/(m s)	54.498 cm/s	325.60 cm/(m s)	31.381 cm/s	37.840 cm/s	0.0713	6.64 10^{-1}	5.43 10^{-1}
	I_F	−177.01 cm/(m s$^{3/4}$)	10.447 cm/s$^{3/4}$	15.0911 cm/(m s$^{3/4}$)	1.4544 cm/s$^{3/4}$	1.7538 cm/s$^{3/4}$	0.9787	1.33 10^{-3}	1.15 10^{-5}
	I_H	−246.15 cm/m	25.731 cm	53.953 cm/m	5.2000 cm	6.2703 cm	0.8740	1.98 10^{-2}	1.29 10^{-3}

(*): Regression with positive correlation.

degrees of freedom. The right-tail probability of the test statistic, denoted by αF, is the significance level of the test. An αF-value less than 0.05 is commonly associated with the significance of the regression. In contrast to R^2, which only depends on *SSreg* and *SSreg* − it is the ratio *SSreg*/(*SSreg* + *SSres*) − the αF-value also accounts for the sample size *n*. The αF-values of the regressions are reported in Table 4 as well. It could be noticed that the regressions of the extensional earthquakes (L'Aquila and Amatrice-Norcia) have moderate R^2 and large sample size, resulting

Table 10
Regressions of intensity measures vs. w, Amatrice-Norcia, October 30th, 2016, $w \leq -0.010$ m, $n = 5$.

Direction		a	b	SE(a)	SE(b)	SE(y)	R^2	α_F	α_{LR}
Horizontal	PGA(*)	156.05 cm/(m s^2)	765.36 cm/s^2	411.88 cm/(m s^2)	188.19 cm/s^2	220.99 cm/s^2	0.0457	7.30 10^{-1}	6.29 10^{-1}
	PGV	−27.597 cm/(m s)	51.523 cm/s	27.961 cm/(m s)	12.776 cm/s	15.003 cm/s	0.2451	3.96 10^{-1}	2.36 10^{-1}
	IV	−66.057 cm/(m s)	70.703 cm/s	62.356 cm/(m s)	28.491 cm/s	33.457 cm/s	0.2722	3.67 10^{-1}	2.07 10^{-1}
	I_A	−67.665 cm/(m s)	473.06 cm/s	519.16 cm/(m s)	237.21 cm/s	278.56 cm/s	0.0056	9.05 10^{-1}	8.67 10^{-1}
	I_F	−52.076 cm/(m s$^{3/4}$)	79.717 cm/s$^{3/4}$	42.688 cm/(m s$^{3/4}$)	19.505 cm/s$^{3/4}$	22.904 cm/s$^{3/4}$	0.3316	3.10 10^{-1}	1.56 10^{-1}
	I_H	−195.82 cm/m	112.44 cm	77.507 cm/m	35.414 cm	41.586 cm	0.6803	8.57 10^{-2}	1.69 10^{-2}
Vertical	PGA	−84.712 cm/(m s^2)	716.03 cm/s^2	344.36 cm/(m s^2)	157.34 cm/s^2	184.77 cm/s^2	0.0198	8.22 10^{-1}	7.52 10^{-1}
	PGV	−56.679 cm/(m s)	18.205 cm/s	18.317 cm/(m s)	8.3693 cm/s	9.8280 cm/s	0.7614	5.35 10^{-2}	7.43 10^{-3}
	IV	−77.322 cm/(m s)	15.990 cm/s	22.681 cm/(m s)	10.363 cm/s	12.170 cm/s	0.7948	4.22 10^{-2}	4.89 10^{-3}
	I_A	−310.21 cm/(m s)	191.88 cm/s	237.52 cm/(m s)	108.53 cm/s	127.44 cm/s	0.3625	2.83 10^{-1}	1.34 10^{-1}
	I_F	−101.08 cm/(m s$^{3/4}$)	26.591 cm/s$^{3/4}$	32.057 cm/(m s$^{3/4}$)	14.647 cm/s$^{3/4}$	17.200 cm/s$^{3/4}$	0.7682	5.11 10^{-2}	6.86 10^{-3}
	I_H	−133.58 cm/m	64.740 cm	48.216 cm/m	22.031 cm	25.870 cm	0.7190	6.95 10^{-2}	1.18 10^{-2}

(*): Regression with positive correlation.

Table 11
Regressions of intensity measures vs. w, L'Aquila, April 6th, 2009, and Amatrice-Norcia, October 30th, 2016, $w \leq -0.010$ m, $n = 10$.

Direction		a	b	SE(a)	SE(b)	SE(y)	R^2	α_F	α_{LR}
Horizontal	PGA	−192.29 cm/(m s^2)	547.21 cm/s^2	291.26 cm/(m s^2)	96.174 cm/s^2	213.65 cm/s^2	0.0517	5.28 10^{-1}	3.20 10^{-1}
	PGV	−47.547 cm/(m s)	39.694 cm/s	16.257 cm/(m s)	5.3679 cm/s	11.925 cm/s	0.5167	1.92 10^{-2}	7.00 10^{-3}
	IV	−87.154 cm/(m s)	58.278 cm/s	30.666 cm/(m s)	10.126 cm/s	22.494 cm/s	0.5024	2.17 10^{-2}	8.24 10^{-3}
	I_A	−482.40 cm/(m s)	222.63 cm/s	303.53 cm/(m s)	100.22 cm/s	222.64 cm/s	0.2400	1.51 10^{-1}	9.76 10^{-2}
	I_F	−76.625 cm/(m s$^{3/4}$)	65.177 cm/s$^{3/4}$	24.700 cm/(m s$^{3/4}$)	8.1560 cm/s$^{3/4}$	18.118 cm/s$^{3/4}$	0.5461	1.46 10^{-2}	4.94 10^{-3}
	I_H	−195.60 cm/m	113.74 cm	42.924 cm/m	14.173 cm	31.486 cm	0.7219	1.86 10^{-3}	3.47 10^{-4}
Vertical	PGA	−583.53 cm/(m s^2)	419.28 cm/s^2	277.87 cm/(m s^2)	91.753 cm/s^2	203.83 cm/s^2	0.3554	6.89 10^{-2}	3.61 10^{-2}
	PGV	−69.214 cm/(m s)	11.197 cm/s	9.5632 cm/(m s)	3.1577 cm/s	7.0148 cm/s	0.8675	8.90 10^{-5}	6.93 10^{-6}
	IV	−83.764 cm/(m s)	11.918 cm/s	12.394 cm/(m s)	4.0926 cm/s	9.0915 cm/s	0.8509	1.40 10^{-4}	1.28 10^{-5}
	I_A	−520.61 cm/(m s)	67.497 cm/s	141.09 cm/(m s)	46.587 cm/s	103.49 cm/s	0.6299	6.13 10^{-3}	1.62 10^{-3}
	I_F	−117.25 cm/(m s$^{3/4}$)	17.799 cm/s$^{3/4}$	15.861 cm/(m s$^{3/4}$)	5.2374 cm/s$^{3/4}$	11.635 cm/s$^{3/4}$	0.8723	7.68 10^{-5}	5.72 10^{-6}
	I_H	−179.11 cm/m	39.105 cm	28.156 cm/m	9.2971 cm	20.653 cm	0.8349	2.18 10^{-4}	2.19 10^{-5}

in very small αF-values and high level of significance. The contractional earthquake (Emilia) has low R^2 and medium sample size, resulting again in an αF-value less than 0.05, indicating the significance of the regression.

As an alternative to the F-test, the likelihood ratio (LR) test can be performed. It can be shown that the classical least squares estimation of the parameters of the regression is equivalent to the maximum likelihood estimation, assuming that the dependent variable be normally distributed with mean equal to $ax + b$ and standard deviation equal to σ. The parameter set θ contains a, b and σ. To appraise the parameters, the maximum likelihood estimation (Benjamin and Cornell, 1970) is used, whereby the parameters of the model are obtained by maximizing the likelihood function $L(\theta)$, so that, under the assumed statistical model, the observed data is most probable.

In order to assess the significance of the regression, the likelihood-ratio (LR) test was carried out, by removing from the initial statistical model the coefficient a, thus assuming that no relation be present between the dependent and the independent variable. The null hypothesis, i.e., the coefficient a cannot be removed, is then checked according to the LR test (Neyman and Pearson, 1933). In fact, the LR test assesses the goodness of fit of two competing statistical models based on the ratio of their likelihoods, specifically one found by maximization over the entire parameter space Θ and another constraining the parameters in a subspace Θ_0 of Θ. In the case at hand, Θ contains all the coefficients a, b and σ, whereas Θ_0 only contains b and σ. If the null hypothesis is supported by the observed data, the two likelihoods should differ by more than a threshold. The LR test statistic can be expressed as:

Table 12
Regressions of intensity measures vs. w, Emilia, May 29th, 2012, $w \geq 0.010$ m, $n = 18$.

Direction		a	b	SE(a)	SE(b)	SE(y)	R^2	α_F	α_{LR}
Horizontal	*PGA*	1148.67 cm/(m s^2)	175.91 cm/s^2	814.50 cm/(m s^2)	61.110 cm/s^2	108.74 cm/s^2	0.1106	1.78 10^{-1}	1.46 10^{-1}
	PGV	367.44 cm/(m s)	6.5397 cm/s	116.18 cm/(m s)	8.7167 cm/s	15.510 cm/s	0.3847	6.03 10^{-3}	3.11 10^{-3}
	IV	424.88 cm/(m s)	17.630 cm/s	180.53 cm/(m s)	13.545 cm/s	24.102 cm/s	0.2572	3.17 10^{-2}	2.07 10^{-2}
	I_A	619.60 cm/(m s)	44.257 cm/s	412.25 cm/(m s)	30.931 cm/s	55.037 cm/s	0.1237	1.52 10^{-1}	1.23 10^{-1}
	I_F	590.22 cm/(m s$^{3/4}$)	11.270 cm/s$^{3/4}$	180.56 cm/(m s$^{3/4}$)	13.547 cm/s$^{3/4}$	24.105 cm/s$^{3/4}$	0.4004	4.83 10^{-3}	2.41 10^{-3}
	I_H	1086.70 cm/m	32.457 cm	423.61 cm/m	31.783 cm	56.553 cm	0.2914	2.08 10^{-2}	1.28 10^{-2}
Vertical	*PGA*	4063.35 cm/(m s^2)	15.117 cm/s^2	1439.29 cm/(m s^2)	107.99 cm/s^2	192.15 cm/s^2	0.3325	1.22 10^{-2}	6.99 10^{-3}
	PGV	137.48 cm/(m s)	−1.0814 cm/s	49.495 cm/(m s)	3.7135 cm/s	6.6076 cm/s	0.3253	1.34 10^{-2}	7.78 10^{-3}
	IV	115.13 cm/(m s)	0.50303 cm/s	38.819 cm/(m s)	2.9125 cm/s	5.1824 cm/s	0.3547	9.11 10^{-3}	4.98 10^{-3}
	I_A	1100.12 cm/(m s)	−13.691 cm/s	504.72 cm/(m s)	37.868 cm/s	67.381 cm/s	0.2290	4.46 10^{-2}	3.05 10^{-2}
	I_F	201.81 cm/(m s$^{3/4}$)	−0.85513 cm/s$^{3/4}$	74.521 cm/(m s$^{3/4}$)	5.5912 cm/s$^{3/4}$	9.9487 cm/s$^{3/4}$	0.3143	1.55 10^{-2}	9.16 10^{-3}
	I_H	220.86 cm/m	5.4120 cm	76.632 cm/m	5.7496 cm	10.231 cm	0.3417	1.08 10^{-2}	6.08 10^{-3}

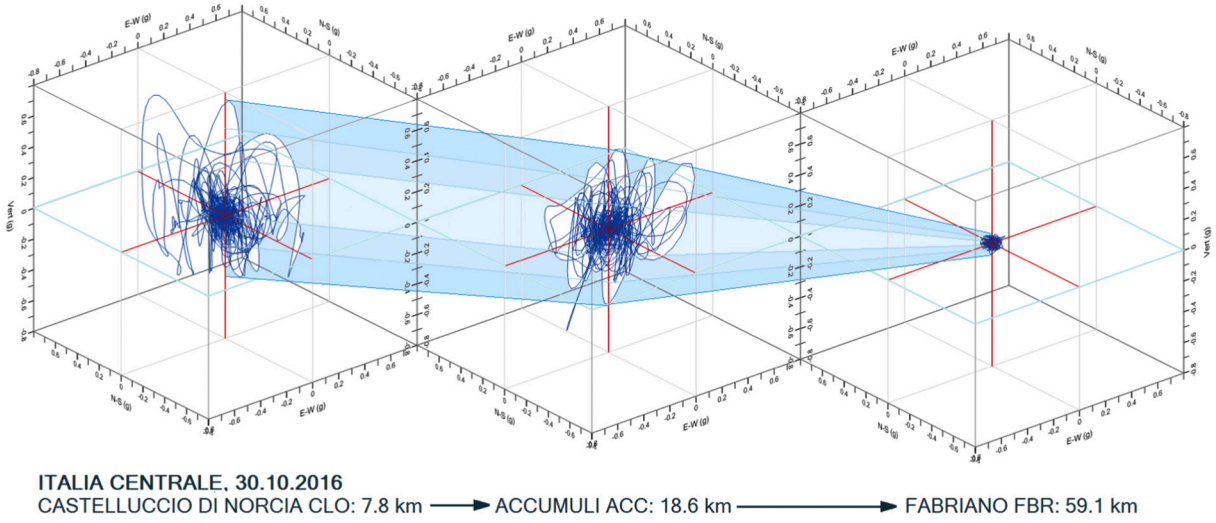

Fig. 4. Acceleration trajectories generated during the M_w 6.5 October 30th 2016 of the Amatrice-Norcia seismic sequence after Mariani and Pugi (2019) showing high peak ground accelerations in the two boxes to the left within the epicentral area above the active volume, moving along strike at 7.8 km, 18.6 km from the epicentre, where the coseismic ground shaking has been maximum. In the far-field above the passive volume at 59.1 km distance from the epicentre, the PGA is instead drastically buffered. Notice the relevant vertical and horizontal acceleration vectors in the two stations above the active volume.

$$\lambda = -2ln\left[\frac{sup_{\theta\in\Theta_0}\, L(\theta)}{sup_{\theta\in\Theta}\, L(\theta)}\right] \tag{2}$$

where, in the case at hand, $\sup_{\theta\in\Theta 0}\, L(\theta)$ represents the likelihood maximized over the subspace Θ_0, and $\sup_{\theta\in\Theta}\, L(\theta)$ the likelihood maximized over the complete initial space Θ. The test statistic can also be expressed as a difference between the log-likelihoods:

$$\lambda = -2(\ell_0 - \ell) \tag{3}$$

where:

$$\ell_0 = ln\left[sup_{\theta\in\Theta_0}\, L(\theta)\right] \tag{4a}$$

$$\ell = ln\left[sup_{\theta\in\Theta}\, L(\theta)\right] \tag{4b}$$

If the null hypothesis is true, Wilks' theorem ensures that λ converges asymptotically, for large samples, to a chi-square (χ^2) distribution with k degrees of freedom, equal to the difference in dimensionality between Θ and Θ_0 (Wilks, 1938). In the case at hand $k = 1$.

When a large difference occurs between the likelihood maximized over the complete space Θ and the likelihood maximized over the subspace Θ_0, the value assumed by λ is large, its right-tail probability α_{LR} is small, and the null hypothesis is accepted, i.e., the coefficient a cannot be removed from the regression. An α_{LR}-value less than or equal to 0.05 is commonly interpreted as justification for accepting the null hypothesis, i.e., there is a significant difference between the complete and the reduced model, thus not allowing the removal of the coefficient a from the model. The α_{LR} -values of the regressions are reported in Table 4. It can be noticed that they are lower than the corresponding α_F -values, thus confirming the significance of the regressions.

To further assess the reliability of the proposed procedure, an investigation of the confidence bounds of the regressions was carried

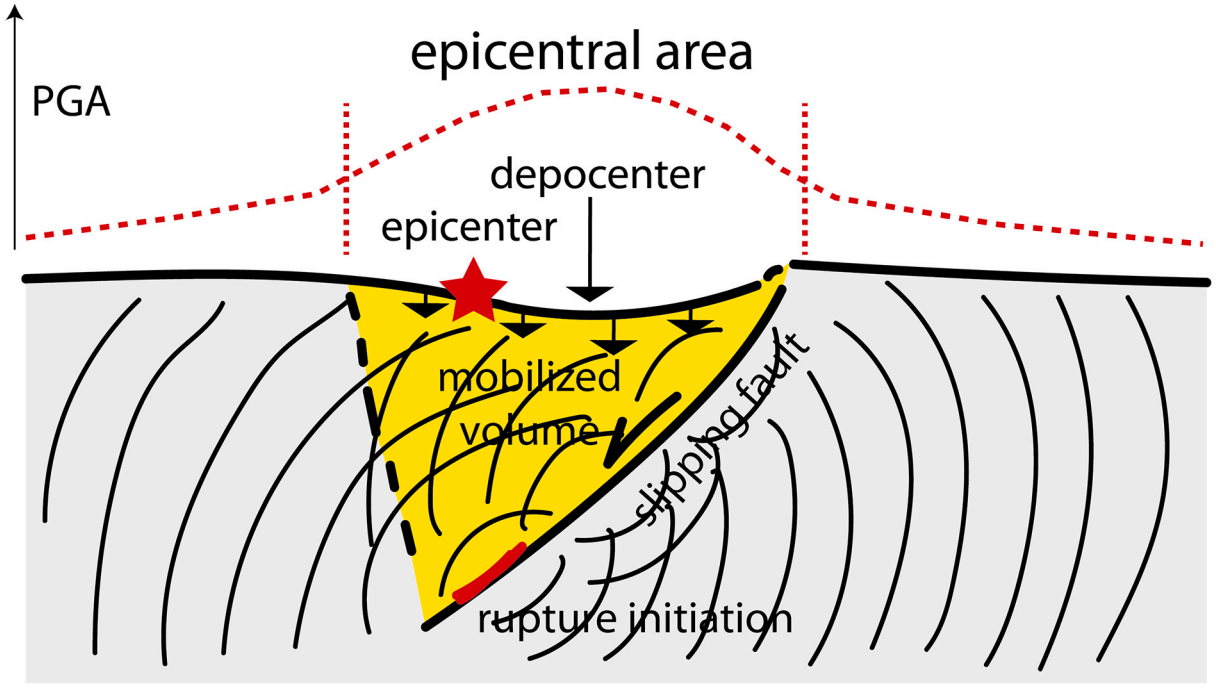

Fig. 5. Cartoon illustrating the overlap of the hanging wall volume undergoing coseismic subsidence and contemporaneously crossed by the seismic waves sourced by the normal fault slip. In the 'active' volume where the two phenomena overlap, the peak ground acceleration (PGA) is maximum, and it may be referred to as the epicentral area. Outside the mobilized volume, seismic waves propagate into a 'passive', i.e., static volume. This may explain the higher macroseismic intensity at the surface of the active volume.

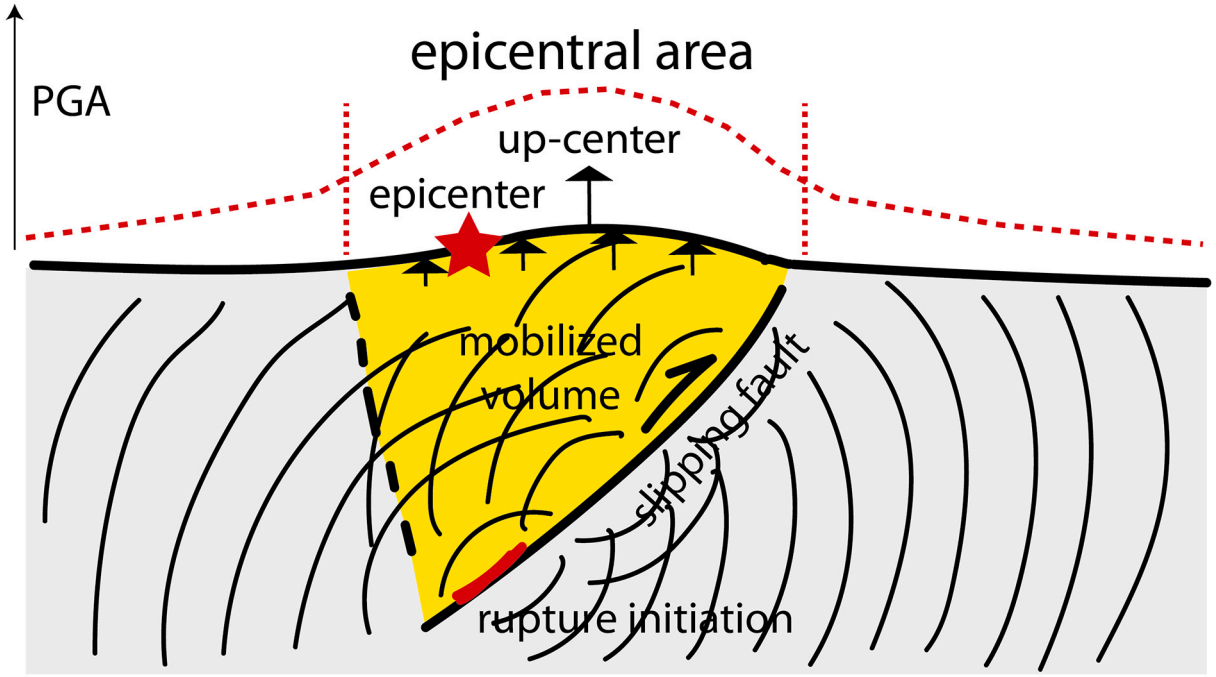

Fig. 6. Cartoon illustrating the overlap of the hanging wall volume undergoing coseismic uplift and contemporaneously crossed by the seismic waves sourced by the slip along with the thrust. In the 'active' volume where the two phenomena overlap, the peak ground acceleration (PGA) is maximum, and it may be referred to as the epicentral area. Outside the mobilized volume, seismic waves propagate into a 'passive', i.e., static volume. This may explain the higher macroseismic intensity at the surface of the active volume.

out. A confidence bound is an interval estimate of the mean value computed from the statistics of the observed data, and its width provides an idea of the uncertainty about its estimation. It has an associated confidence level that quantifies the level of confidence that the mean value lies in such an interval. The lower the confidence level specified, the larger the estimated range that is likely to contain the line. The confidence level was chosen equal to 0.05, meaning that there is a 95% probability that the linear regression line of the population will lie within the confidence bound computed from the sample data (Ross, 2004). Confidence bounds are shown in Fig. 7 by dashed lines. It can be

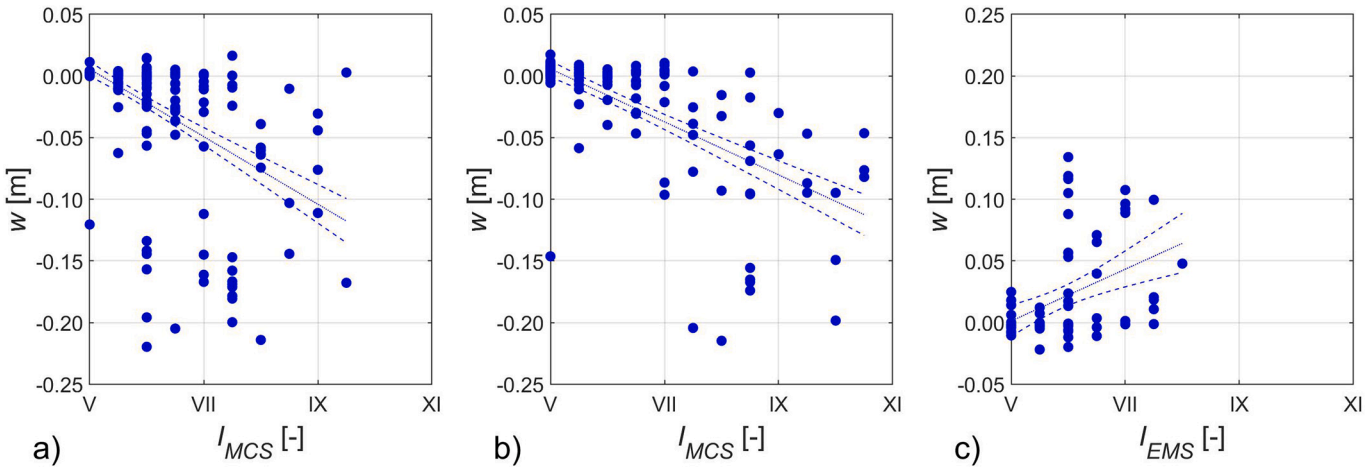

Fig. 7. Regressions of DInSAR displacement vs. macroseismic intensity: a) L'Aquila, 2009, earthquake, b) Amatrice-Norcia, 2016, earthquake, c) Emilia, 2012, earthquake.

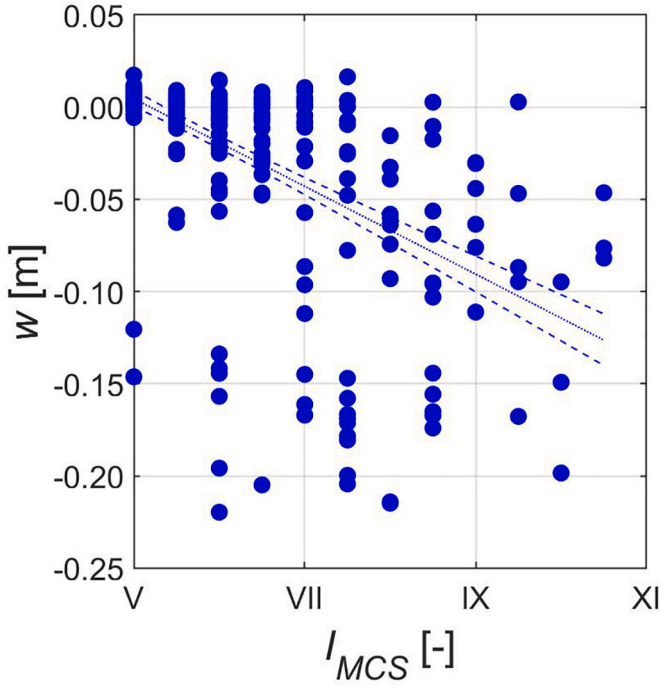

Fig. 8. Regression of DInSAR displacement vs. macroseismic intensity for L'Aquila, 2009 and Amatrice-Norcia, 2016 earthquakes.

noticed that the regressions have tight confidence bounds, especially in the case of the extensional earthquakes (L'Aquila and Amatrice-Norcia) and low intensities, where intensity data are more numerous. At high intensities the width of the confidence bounds remains in any case limited (±0.025 mm) for all the three earthquakes.

Since a certain degree of conventionality is unavoidable in intensity assignment, which is anyway based on an expert judgment, inverse regressions (I_{MCS} - w), i.e., computing the errors along the direction of the intensity axis, were calculated as well, and reported in Table 4, where $y = I_{MCS}$ or I_{EMS}, $x = w$.

It can be noticed that similar coefficients hold for the earthquakes with normal mechanisms, namely L'Aquila and Amatrice-Norcia. A unique relationship can be established for these earthquakes, whose regression coefficients are reported in Table 5. As expected, the regression coefficients, the determination coefficient and the SE on the dependent variables are intermediate between the corresponding values reported in Table 4, whereas the SE on the coefficients a and b, the α_F-value and the α_{LR}-value are lower. The regression w - I_{MCS} is also shown in Fig. 8, along with its confidence bounds.

6. Relations between DInSAR vertical ground deformation and ground motion intensity measures

A second group of empirical relations links DInSAR vertical ground deformation to ground motion intensity measures. Since ground motion intensities are measured only at the stations, DInSAR data were spatially interpolated to calculate the vertical displacement at the stations. Ground motion intensity measures, as opposed to macroseismic intensities, are continuous quantities, are not affected by the intrinsic scatter related to structural response, by the conventional estimation of damage and vulnerability, and by damage cumulation.

On the other hand, the number of records in sites experiencing significant non-zero residual displacements is rather limited: $n = 5$ for the L'Aquila earthquake, $n = 5$ for the Amatrice-Norcia earthquake and $n = 18$ for the Emilia earthquake. Regarding the Amatrice-Norcia earthquake, the analysis was performed for the shock on October 30th, 2016, M_w 6.5, because of the larger availability of data due to the mobile accelerometric network (Luzi et al., 2017). DInSAR data cumulate the effects of the shocks of October 26th and 30th.

Different ground motion intensity measures are considered, calculated from corrected horizontal accelerograms. Peak ground acceleration (*PGA*) and peak ground velocity (*PGV*) are selected as ground motion parameters because they are the most used intensity measures.

Another velocity measure is the maximum incremental velocity (*IV*), given by the area below the largest acceleration pulse (Anderson and Bertero, 1987). Peak ground displacement (*PGD*) is not considered in this study because of the correction procedure consisting of baseline correction, non-causal 2nd order high-pass and low-pass Butterworth filter, cosinusoidal taper and removal of linear displacement drift (Luzi et al., 2017). The effect of this procedure is a final displacement equal to zero, which contrasts with physical evidence and DInSAR data. Further confirmation of non-zero final displacement is provided by high-frequency GPS records (Wilkinson et al., 2017).

Among instrumental intensity measures, Arias, Fajfar and Housner Intensities are taken into consideration. Arias Intensity (I_A) (Arias, 1970) is given by:

$$I_A = \frac{\pi}{2g}\int_0^{\infty} a_g^2(t)\mathrm{d}t \tag{5}$$

where a_g is ground acceleration and t time. Arias Intensity, which dimensionally is a velocity, can be correlated to damage (Cabañas et al.,

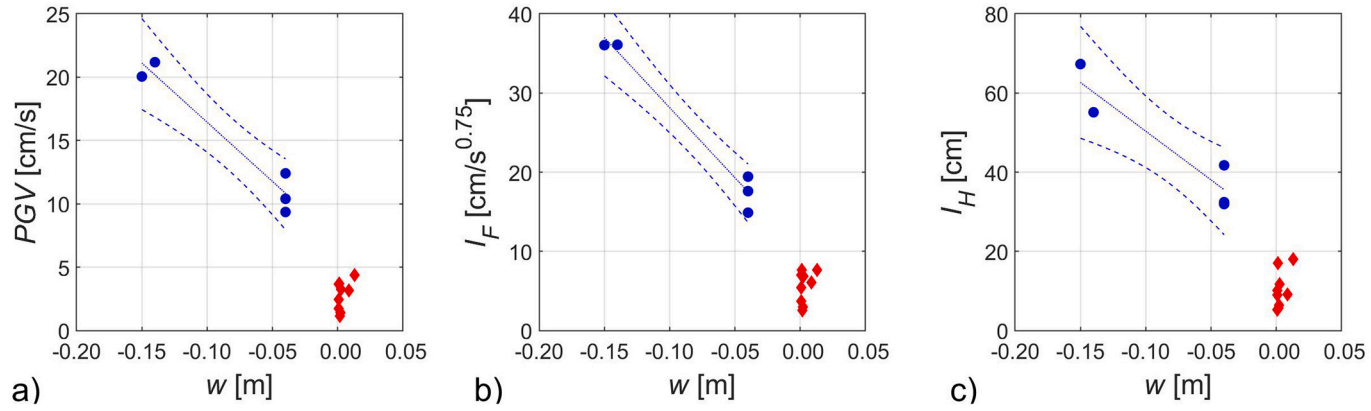

Fig. 9. Regressions of intensity measures along the vertical direction vs. w, L'Aquila, April 6th, 2009 (blue circles: $w \leq -0.010$ m, red rhombi: $w > -0.010$ m). (For interpretation of the references to colour in this figure legend, the reader is referred to the web version of this article.)

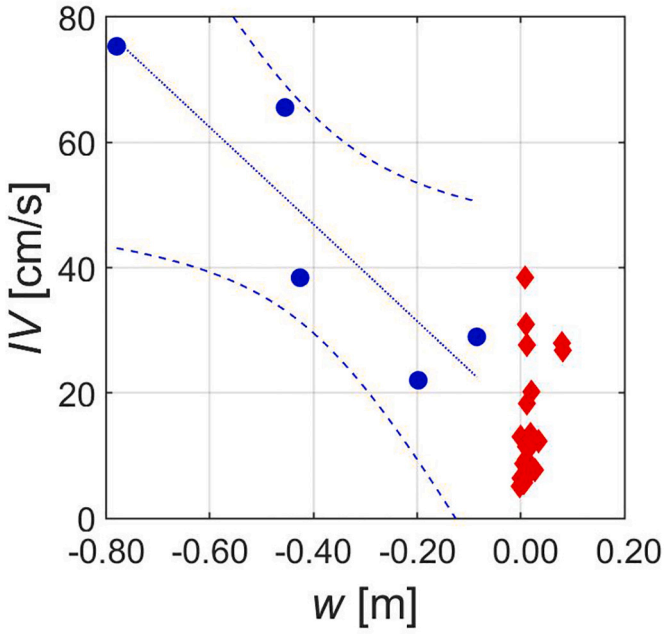

Fig. 10. Regression of IV along the vertical direction vs. w, Amatrice-Norcia, October 30th, 2016 (blue circles: $w \leq -0.010$ m, red rhombi: $w > -0.010$ m). (For interpretation of the references to colour in this figure legend, the reader is referred to the web version of this article.)

1997) but tends to overestimate the intensity of earthquakes with long duration, high acceleration, and broadband frequency content (Uang and Bertero, 1988). Arias Intensity has been demonstrated to be an effective predictor of damage to short-period structures (Stafford et al., 2009).

Fajfar Intensity (I_F) (Fajfar et al., 1990) is defined as:

$$I_F = PGV\, t_D^{0.25} \tag{6}$$

where centimetres and seconds are used, t_D is the Trifunac and Brady strong motion duration (Trifunac and Brady, 1975):

$$t_D = t_{0.95} - t_{0.05} \tag{7}$$

and $t_{0.05}$ and $t_{0.95}$ are the time values at which 5% and 95% of the time integral of the history of squared accelerations are reached, respectively. Fajfar Intensity was formulated to represent earthquake potential to damage medium-period structures.

Finally, Housner Intensity (I_H) (Housner, 1952) is defined as the integral of the elastic pseudo-velocity spectrum, over the period T ranging between 0.1 and 2.5 s:

$$I_H = \int_{0.1}^{2.5} S_{pv}(T\xi = 0.05)\, \mathrm{d}T = \frac{1}{2\pi}\int_{0.1}^{2.5} S_{pa}(T\xi = 0.05) T\, \mathrm{d}T \tag{8}$$

where S_{pv} and S_{pa} are the pseudo-velocity and the pseudo-acceleration, respectively, at undamped natural period T and damping ratio $\xi = 0.05$. Housner Intensity, which dimensionally is a displacement, can be considered as the first moment of the area of S_{pa} ($0.1\ \mathrm{s} \leq T \leq 2.5\ \mathrm{s}$) about the S_{pa} axis. Therefore, it is larger for ground motions with a significant amount of low-frequency content.

The ground motion intensity measures were calculated along the vertical direction and in the horizontal plane. A set of directions in the horizontal plane, with angular step 10°, was considered, the aim being to determine the highest values of horizontal ground motion intensity measures. For each direction, acceleration time history was calculated by projecting the NS and EW components, and ground motion intensity measures were determined.

The ground motion intensity measures, and the corresponding DInSAR displacements, are reported in Table 6 for L'Aquila earthquake, in Table 7 for Amatrice-Norcia earthquake and in Table 8 for Emilia earthquake. Only displacements $w \leq -0.010$ m are considered in the analyses for L'Aquila and Amatrice-Norcia earthquakes, and displacements $w \geq 0.010$ m for Emilia earthquake.

The regressions of intensity measures vs. w can be written as:

$$y = a\, w + b \ (w \text{ in m}) \tag{9}$$

where $y = PGA, PGV, IV, I_A, I_F, I_H$. The regression coefficients a, b, the SE on a, b, y, the determination coefficients R^2, the α_F-values and the α_{LR}-values for L'Aquila earthquake are reported in Table 9. It can be noticed that many regressions have α_F, $\alpha_{LR} > 0.05$, and high values of SE, because of the small sample size. It can also be noticed that the regressions of PGA have positive correlation, i.e., low PGA values correspond to low w values, which is physically meaningless. Only the regression of PGV, I_F and I_H along the vertical direction, characterized by high R^2, can be considered significant from the statistical point of view, according to their α_F- values. Since, for all the regressions, $\alpha_{LR} < \alpha_F$, the significance of the regressions was cautiously based on α_F. These regressions are shown in Fig. 9, where also the records with $w > -0.010$ m are reported, which were not considered in the analyses and are concentrated at low values of the intensity measures. Although the determination coefficient is high, the confidence bounds are rather wide, due to the small sample size.

The results for Amatrice-Norcia earthquake are reported in Table 10. Only the regression if IV along the vertical direction has $\alpha_F < 0.05$. This regression is shown in Fig. 10, where the records with $w > -0.010$ m are

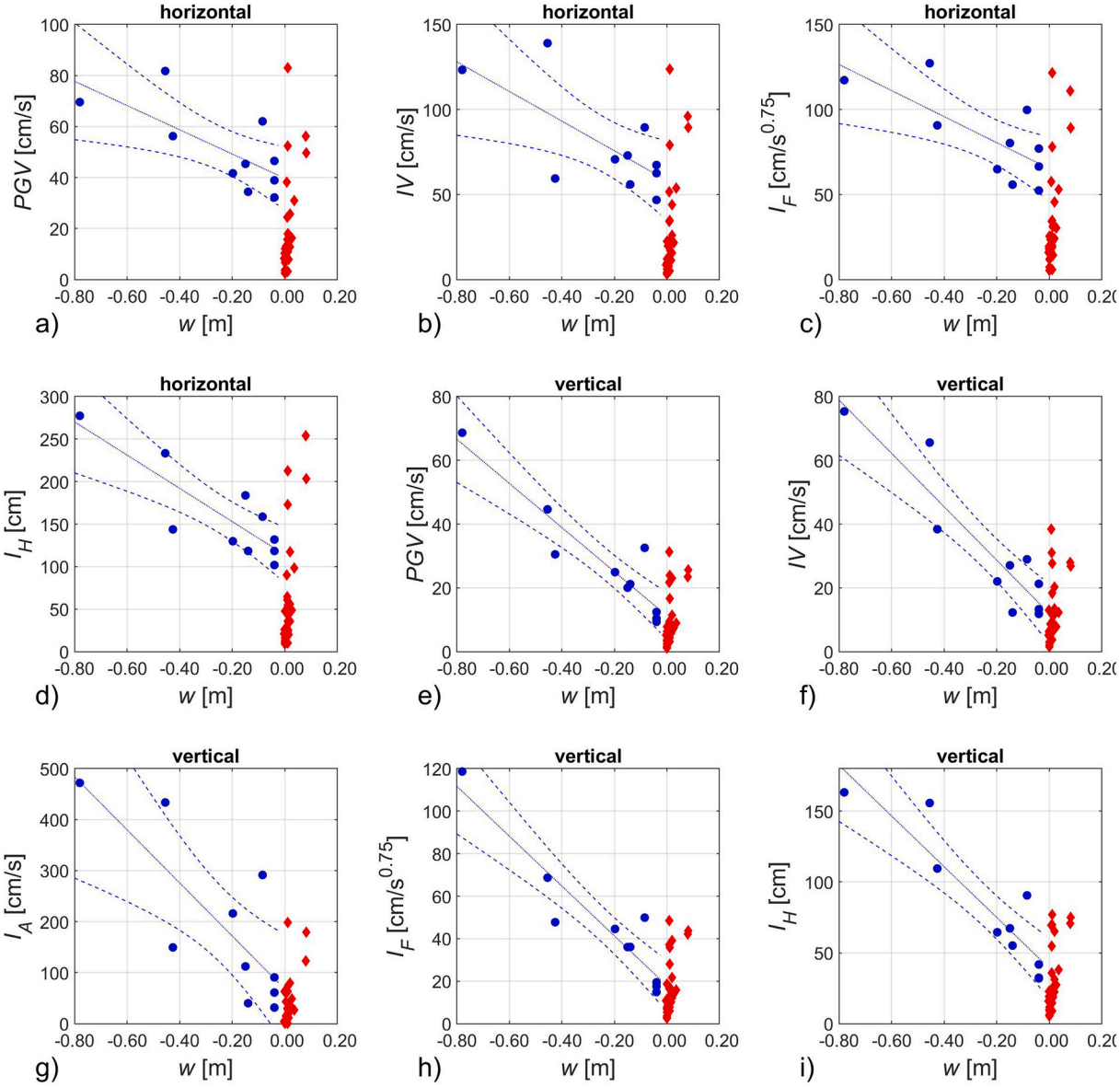

Fig. 11. Regressions of intensity measures vs. w, L'Aquila, April 6th, 2009, and Amatrice-Norcia, October 30th, 2016 (blue circles: $w \leq -0.010$ m, red rhombi: $w > -0.010$ m). (For interpretation of the references to colour in this figure legend, the reader is referred to the web version of this article.)

also reported. The latter were not considered in the analysis and are mainly concentrated at low values of *IV*, although with significant scatter. Other regressions with high R^2, and α_F-values near the critical value of 0.05, are that of I_H in the horizontal plane and those of *PGV*, I_F and I_H along the vertical direction.

The results for the set of L'Aquila and Amatrice-Norcia earthquakes are reported in Table 11 and show a general improvement compared to the individual earthquakes. It can be noticed that positive correlations are no longer present, and several regressions have $\alpha_F < 0.05$, namely those of *PGV*, *IV*, I_F, I_H in the horizontal plane and those of *PGV*, *IV*, I_A, I_F, I_H along the vertical direction. These regressions, along with their confidence bounds, are shown in Fig. 11, where also the records with $w > -0.010$ m are reported. The latter are concentrated at low values of the intensity measures, although with significant scatter, especially for the intensity measures in the horizontal plane. For all the regressions, $\alpha_{LR} < \alpha_F$. As expected, w is better correlated with the intensity measures along the vertical direction, as well as with the intensity measures related to medium and low frequencies (*PGV*, *IV*, I_F, I_H), compared to those related to high frequencies (*PGA*, I_A). Regarding Housner Intensity in the horizontal plane, studies in literature (Decanini et al., 2002; Marotta et al., 2018; Masi et al., 2011) demonstrated that it can be a valid alternative to other seismic peak parameters. The confidence bounds widen for $w \leq -0.400$ m, that is for very large displacements for the Italian seismicity, due the small number of samples.

The results for the Emilia earthquake are reported in Table 12. The regressions of *PGV*, *IV*, I_F, I_H in the horizontal plane and all the regressions along the vertical direction have $\alpha_F < 0.05$. These regressions are also shown in Fig. 12. The regression of the vertical I_A, whose α_F-value is close to 0.05, is omitted. They have higher scatter, lower R^2 and wider confidence bounds compared to those of the set of L'Aquila and Amatrice-Norcia earthquakes. The results confirm that w is better correlated with the intensity measures along the vertical component, as well as with the intensity measures related to medium and low frequencies.

7. Discussion

DInSAR data provide powerful tools for improving seismic hazard

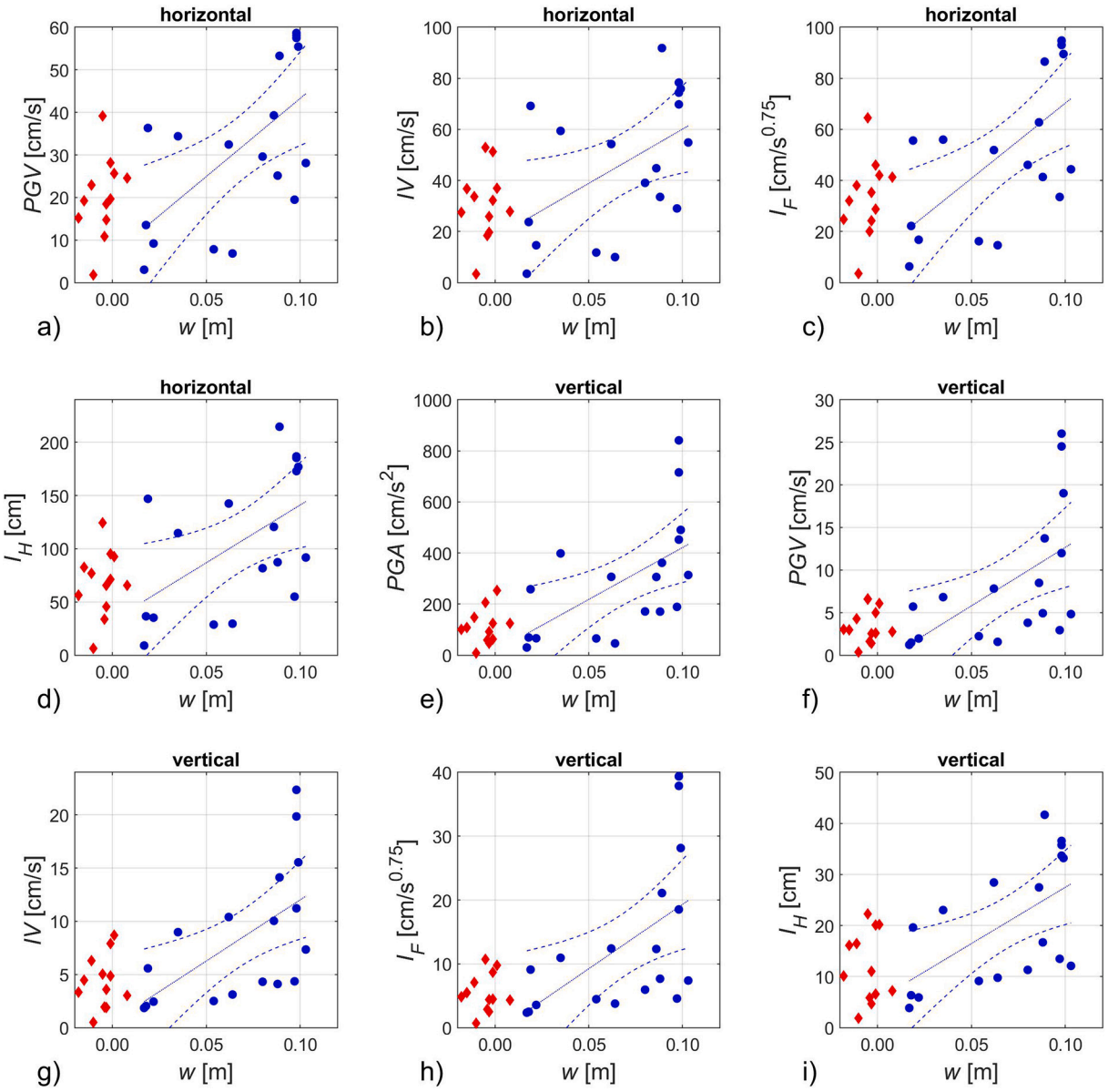

Fig. 12. Regressions of intensity measures vs. w, Emilia, May 29th, 2012 (blue circles: $w \geq 0.010$ m, red rhombi: $w < 0.010$ m). (For interpretation of the references to colour in this figure legend, the reader is referred to the web version of this article.)

assessment (Gürpinar et al., 2017; Livio et al., 2017). The good quality of DInSAR, accelerometric and macroseismic data of Italy allows to infer some innovative evaluation of the relationship between earthquakes and damage concentration in the epicentral areas. It is well known that the main source of damage to structures is the shaking in the horizontal plane. However, in extensional and contractional earthquakes the horizontal and vertical components are correlated in the near field (Ambraseys and Douglas, 2003). This study investigated whether the residual vertical displacement measured by DInSAR in the active zone can be exploited as an indicator for macroseismic intensity and instrumental intensity measures. It may be argued how the analyses presented are specific only for the three analyzed earthquakes and therefore, they cannot be immediately generalized to other case studies for ground motion prediction aims. However, considerations on up-to-date databases from GNSS (e.g., Ruhl et al., 2019) as well as from strong-motion recordings (D'Amico et al., 2020, 2021; Schiappapietra et al., 2021) broaden the spectrum of applications addressed here. In extensional and contractional tectonic settings, the near field areas tend to be elliptical and concentrated in the hanging wall where the vertical component (coseismic subsidence and uplift, respectively) is in average about ten times higher than that of opposite sign in the footwall or hanging wall itself. The near field covers areas of 300–600 km^2 for a range of M_w 6–6.9. They are zones where the highest seismic hazard has to be expected, apart from areas of site amplification that may occur also outside the epicentral zone (Petricca et al., 2021). One explanation is the contemporaneous movement of the hanging wall and the passage of seismic waves delivered by the friction on the fault plane. Within this volume may form trapped waves and rupture directivity (Kawase, 1996; Calderoni et al., 2012, 2017), which may amplify and reverberate. Therefore, the movement and the high vertical accelerations affecting the hanging wall allow stronger horizontal accelerations, hence provoking the greatest shaking within the activated volume (Figs. 5 and 6) and the higher *PGA* in the epicentral area that is not necessarily near the fault plane, but rather in the active domain, i.e., the area undergoing the higher vertical (either subsidence or uplift) coseismic deformation as demonstrated by Petricca et al. (2021). The regression analyses presented in this study clearly show that the area where the macroseismic intensity is greater than or equal to V, i.e., the damage threshold, is

nearly coincident with the active zone where the residual displacement is different than zero, apart from some sites where local amplification occurred. In addition, higher values of the instrumental measures of intensity occur in the active zone, and these are negatively/positively correlated with DInSAR for extensional/contractional earthquakes. More examples of DInSAR and macroseismic data are needed to reach general conclusions. However, the case histories presented here may represent a useful starting point for a better understanding on the relevance of the vertical deformation occurring during the shaking in the epicentral area of an earthquake.

8. Conclusions

The DInSAR data of the three major recent seismic sequences in Italy (L'Aquila 2009, Emilia 2012 and Amatrice-Norcia 2016) allows a quite precise computation of the coseismic ground deformation. In the Amatrice-Norcia (Central Italy) the maximum recorded *PGA* are inside the elongated area that underwent coseismic subsidence, which can be defined as the near field. As soon as we move outside the vertically deformed area, in the so-called far-field, the *PGA* is drastically reduced (Fig. 4). The subsided area coincides with the epicentral area and shows an elliptical shape that corresponds to the surface projection of the upper crustal volume affected by movement in the fault hanging wall. Therefore, this volume is contemporaneously affected by the downward or upward movement and the propagation of the seismic waves generated by the shear on the fault surface. For this reason, this volume is defined as 'active' (Figs. 5 and 6) to be distinguished from the 'passive' volume, which is only crossed by seismic waves, and where the ground motion prediction equations (GMPEs) describe the attenuation of the crust. The comparison of the vertical component of the ground deformation with the macroseismic intensity demonstrates that the most damaged area matches well with the perimeter that underwent the vertical deformation and the highest peak ground acceleration data, apart from some amplification sites that may occur outside the epicentral area. These data confirm how the vertical component of ground motion may determine a transient lowering of strength in masonry with poor mechanical characteristics affected by synchronous horizontal shaking (Liberatore et al., 2019), and still very common in the Italian building stock. The comparisons of the vertical deformation with ground motion intensity measures show a substantial homogeneity of the extensional earthquakes analyzed (L'Aquila and Amatrice-Norcia), whereas the contractional earthquake (Emilia) has significantly different characteristics. Vertical deformation is better correlated with the intensity measures related to medium-long periods (*PGV*, *IV*, Fajfar intensity and Housner intensity), compared to short periods (*PGA*, Arias intensity).

Authors statement

All authors contributed to the article with data, analysis and interpretation.

Declaration of Competing Interest

The authors declare that they have no known competing financial interests or personal relationships that could have appeared to influence the work reported in this paper.

Acknowledgements

We thank Christian Bignami, Paolo Clemente, Valerio De Rubeis and Stefano Pampanin for fruitful discussions. The paper benefited by critical reading of two anonymous referees and the Associate Editor. This work has been partially carried out under the programs "Dipartimento della Protezione Civile – Consorzio RELUIS". The opinions expressed in this publication are those of the authors and are not necessarily endorsed by the Dipartimento della Protezione Civile.

References

Akoglu, A.M., Cakir, Z., Meghraoui, M., Belabbes, S., El Alami, S.O., Ergintav, S., Akyüz, H.S., 2006. The 1994–2004 Al Hoceima (Morocco) earthquake sequence: conjugate fault ruptures deduced from InSAR. Earth Planet. Sci. Lett. 252 (3–4), 467–480. https://doi.org/10.1016/j.epsl.2006.10.010.

Albano, M., Barba, S., Bignami, C., Carminati, E., Doglioni, C., Moro, M., Stramondo, S., Saroli, M., 2021a. Three-dimensional numerical simulation of the interseismic and coseismic phases associated with the 6 April 2009, Mw 6.3 L'Aquila earthquake (Central Italy). Tectonophysics 798, 228685. https://doi.org/10.1016/j.tecto.2020.228685.

Albano, M., Barba, S., Bignami, C., Carminati, E., Doglioni, C., Moro, M., Saroli, M., Samsonov, S., Stramondo, S., 2021b. Numerical modeling of the seismic cycle for normal and reverse faulting earthquakes in Italy. Geophys. J. Int. https://doi.org/10.1093/gji/ggaa608.

Ambraseys, N.N., Douglas, J., 2003. Near-field horizontal and vertical earthquake ground motions. Soil Dyn. Earthq. Eng. 23 (1), 1–18.

Anderson, J.C., Bertero, V.V., 1987. Uncertainties in establishing design earthquakes. J. Struct. Eng. (United States) 113, 1709–1724. https://doi.org/10.1061/(ASCE)0733-9445(1987)113:8(1709).

Arias, A., 1970. A measure of earthquake intensity. In: Seismic Design for Nuclear Power Plants, pp. 438–483.

Atzori, S., Hunstad, I., Chini, M., Salvi, S., Tolomei, C., Bignami, C., Stramondo, S., Trasatti, E., Antonioli, A., Boschi, E., 2009. Finite fault inversion of DInSAR coseismic displacement of the 2009 L'Aquila earthquake (Central Italy). Geophys. Res. Lett. 36 (15) https://doi.org/10.1029/2009GL039293.

Azzaro, R., Tertulliani, A., Bernardini, F., Camassi, R., Del Mese, S., Ercolani, E., Graziani, L., Locati, M., Maramai, A., Pessina, V., Rossi, A., Rovida, A., Albini, P., Arcoraci, L., Berardi, M., Bignami, C., Brizuela, B., Castellano, C., Castelli, V., D'Amico, S., D'Amico, V., Fodarella, A., Leschiutta, I., Piscini, A., Sbarra, M., 2016. Amatrice 2016 earthquake: macro-seismic survey in the damage area and preliminary EMS intensity assessment. Ann. Geophys. https://doi.org/10.4401/ag-7203.

Belabbès, S., Meghraoui, M., Çakir, Z., Bouhadad, Y., 2009. InSAR analysis of a blind thrust rupture and related active folding: the 1999 Ain Temouchent earthquake (M w 5.7, Algeria) case study. J. Seismol. 13 (4), 421–432. https://doi.org/10.1007/s10950-008-9135-x.

Benjamin, J.R., Cornell, C.A., 1970. Probability, Statistics, and Decision for Civil Engineers. McGraw-Hill.

Biggs, J., Wright, T.J., 2020. How satellite InSAR has grown from opportunistic science to routine monitoring over the last decade. Nature Comm. 11 (1), 1–4.

Bignami, C., Valerio, E., Carminati, E., Doglioni, C., Tizzani, P., 2019. Volume unbalance on the 2016 Amatrice - Norcia (Central Italy) seismic sequence and insights on normal fault earthquake mechanism. Sci. Rep. 9, 4250. https://doi.org/10.1038/s41598-019-40958-z.

Bignami, C., Valerio, E., Carminati, E., Doglioni, C., Petricca, P., Tizzani, P., Lanari, R., 2020. Are normal fault earthquakes due to elastic rebound or gravitational collapse? Ann. Geophys. 63 (2), SE213, 2020. https://doi.org/10.4401/ag-8455.

Brunetti, M.T., Peruccacci, S., Rossi, M., Luciani, S., Valigi, D., Guzzetti, F., 2010. Rainfall thresholds for the possible occurrence of landslides in Italy. Nat. Hazards Earth Syst. Sci. 10 (3), 447–458.

Cabañas, L., Benito, B., Herráiz, M., 1997. An approach to the measurement of the potential structural damage of earthquake ground motions. Earthq. Eng. Struct. Dyn. 26, 79–92. https://doi.org/10.1002/(SICI)1096-9845(199701)26:1<79::AID-EQE624>3.0.CO;2-Y.

Calderoni, G., Di Giovambattista, R., Vannoli, P., Pucillo, S., Rovelli, A., 2012. Fault-trapped waves depict continuity of the fault system responsible for the 6 April 2009 Mw 6.3 L'Aquila earthquake, Central Italy. Earth Planet. Sci. Lett. 323, 1–8.

Calderoni, G., Rovelli, A., Di Giovambattista, R., 2017. Rupture directivity of the strongest 2016–2017 Central Italy earthquakes. J. Geophys. Res. Solid Earth 122 (11), 9118–9131.

Carminati, E., Doglioni, C., 2012. Alps vs. Apennines: the paradigm of a tectonically asymmetric Earth. Earth Sci. Rev. 112, 67–96. https://doi.org/10.1016/j.earscirev.2012.02.004.

Cheloni, D., De Novellis, V., Albano, M., Antonioli, A., Anzidei, M., Atzori, S., Avallone, A., Bignami, C., Bonano, M., Calcaterra, S., Castaldo, R., Casu, F., Cecere, G., De Luca, C., Devoti, R., et al., 2017. Geodetic model of the 2016 Central Italy earthquake sequence inferred from InSAR and GPS data. Geophys. Res. Lett. 44 (13), 6778–6787. https://doi.org/10.1002/2017GL073580.

Chiarabba, C., Jovane, L., DiStefano, R., 2005. A new view of Italian seismicity using 20 years of instrumental recordings. Tectonophysics 395 (3–4), 251–268.

D'Amico, M., Felicetta, C., Russo, E., Sgobba, S., Lanzano, G., Pacor, F., Luzi, L., 2020. Italian Accelerometric Archive v 3.1 - Istituto Nazionale di Geofisica e Vulcanologia. Dipartimento della Protezione Civile Nazionale.

D'Amico, M., Schiappapietra, E., Felicetta, C., Sgobba, S., Pacor, F., Lanzano, G., Russo, E., Luzi, L., 2021. NEar-Source Strong-motion flatfile from eBASCO (NESS-eBASCO), version 2.0 (Version 2.0) [Data set]. Istituto Nazionale di Geofisica e Vulcanologia (INGV).

Decanini, L.D., Mollaioli, F., Oliveto, G., 2002. Structural and seismological implications of the 1997 seismic sequence in Umbria and Marche, Italy. In: Oliveto, G. (Ed.), Innovative Approaches to Earthquake Engineering. WIT Press, Southampton, pp. 229–323.

Del Gaudio, V., Wasowski, J., 2004. Time probabilistic evaluation of seismically induced landslide hazard in Irpinia (Southern Italy). Soil Dyn. Earthq. Eng. 24 (12), 915–928.
Devoti, C., Riguzzi, F., Cuffaro, M., Doglioni, C., 2008. New GPS constraints on the kinematics of the Apennines subduction. Earth Planet. Sci. Lett. 273, 163–174.
Devoti, R., D'Agostino, N., Serpelloni, E., Pietrantonio, G., Riguzzi, F., Avallone, A., Cavaliere, A., Cheloni, D., Cecere, G., d'Ambrosio, C., Franco, L., 2017. A combined velocity field of the Mediterranean region. Ann. Geophys. 60 (2), 0215.
Doglioni, C., 1991. A proposal of kinematic modelling for W-dipping subductions - possible applications to the Tyrrhenian - Apennines system. Terra Nova 3 (4), 423–434.
Doglioni, C., 1994. Foredeeps versus subduction zones. Geology 22 (3), 271–274.
Doglioni, C., Carminati, E., Petricca, P., Riguzzi, F., 2015. Normal fault earthquakes or graviquakes. Sci. Rep. 5, 12110. https://doi.org/10.1038/srep12110.
Evangelista, L., Landolfi, L., d'Onofrio, A., et al., 2016. The influence of the 3D morphology and cavity network on the seismic response of Castelnuovo hill to the 2009 Abruzzo earthquake. Bull. Earthq. Eng. 14, 3363–3387. https://doi.org/10.1007/s10518-016-0011-8.
Fajfar, P., Vidic, T., Fischinger, M., 1990. A measure of earthquake motion capacity to damage medium-period structures. Soil Dyn. Earthq. Eng. 9, 236–242. https://doi.org/10.1016/S0267-7261(05)80002-8.
Fiorentino, G., Forte, A., Pagano, E., Sabetta, F., Baggio, C., Lavorato, D., Nuti, C., Santin, S., 2018. Damage patterns in the town of Amatrice after August 24th 2016 Central Italy earthquakes. Bull. Earthq. Eng. 16, 1399–1423.
Galli, P., Camassi, R., Azzaro, R., Bernardini, F., Castenetto, S., Molin, D., Peronace, E., Rossi, A., Vecchi, M., Tertulliani, A., 2009. Terremoto de L'Aquila del 6 aprile 2009: distribuzione delle intensità macrosismiche ed implicazioni sismotettoniche. Il Quaternario 22 (2), 235–246.
Galli, P., Peronace, E., Bramerini, F., Castenetto, S., Naso, G., Cassone, F., Pallone, F., 2016. The MCS intensity distribution of the devastating 24 august 2016 earthquake in central Italy (Mw6.2). Ann. Geophys. 59 https://doi.org/10.4401/ag-7287. FastTrack 5.
Graziani, L., Tertulliani, A., Maramai, A., Rossi, A., Arcoraci, L., 2017. The 1984 Abruzzo- Latium seismic sequence: reappraisal of the existing macroseismic datasets according to the EMS98. J. Seismol. 21 (1), 1–9. https://doi.org/10.1007/s10950-017-9663-3.
Graziani, L., Del Mese, S., Tertulliani, A., Arcoraci, L., Maramai, A., Rossi, A., 2019. Macroseismic assessment (EMS-98) of damage progression during the 2016 17 seismic sequence in Central Italy. Bull. Earthq. Eng. https://doi.org/10.1007/s10518-019-00645-w.
Grimaz, S., Malisan, P., 2017. How could cumulative damage affect the macroseismic assessment? Bull. Earthq. Eng. 15 (6), 2465–2481. https://doi.org/10.1007/s10518-016-0016-3.
Grünthal, G. (Ed.), 1998. European Macroseismic Scale 1998 (EMS-98). European Seismological Commission, sub commission on Engineering Seismology, Working Group Macroseismic Scales. Conseil de l'Europe, Cahiers du Centre Europen de Godynamique et de Sismologie 15, Luxembourg.
Guglielmino, F., Anzidei, M., Briole, P., Elias, P., Puglisi, G., 2013. 3D displacement maps of the 2009 L'Aquila earthquake (Italy) by applying the SISTEM method to GPS and DInSAR data. Terra Nova 25 (1), 79–85. https://doi.org/10.1111/ter.12008.
Gürpinar, A., Serva, L., Livio, F., Rizzo, P.C., 2017. Earthquake-induced crustal deformation and consequences for fault displacement hazard analysis of nuclear power plants. Nuclear Eng. Des. 311, 69–85.
Hernandez, B., Cocco, M., Cotton, F., Stramondo, S., Scotti, O., Courboulex, F., Campillo, M., 2004. Rupture history of the 1997 Umbria-Marche (Central Italy) main shocks from the inversion of GPS, DInSAR and near field strong motion data. Ann. Geophys. 47 (4) https://doi.org/10.4401/ag-3349.
Housner, G.W., 1952. Spectrum intensities of strong motion earthquakes. In: Proceedings of the Symposium of Earthquake and Blast Effects on Structures. EERI, Los Angeles, California, pp. 21–36.
ISPRA, 2007. Rapporto Sulle Frane in Italia, p. 78. ISBN 978-88-448-0310-0. https://www.isprambiente.gov.it/it/pubblicazioni/rapporti/Rapporto-sulle-frane-in-Italia.
Kawase, H., 1996. The cause of the damage belt in Kobe: "The basin-edge effect," constructive interference of the direct S-wave with the basin-induced diffracted/Rayleigh waves. Seismol. Res. Lett. 67 (5), 25–34.
Kuang, J., Ge, L., Metternicht, G.I., Ng, A.H.M., Wang, H., Zare, M., Kamranzad, F., 2019. Coseismic deformation and source model of the 12 November 2017 Mw 7.3 Kermanshah Earthquake (Iran–Iraq border) investigated through DInSAR measurements. Int. J. Rem. Sens. 40 (2), 532–554. https://doi.org/10.1080/01431161.2018.1514542.
Lanari, R., Berardino, P., Bonano, M., Casu, F., Manconi, A., Manunta, M., Manzo, M., Pepe, A., Pepe, S., Sansosti, E., Solaro, G., Tizzani, P., Solaro, G., 2010. Surface displacements associated with the L'Aquila 2009 Mw 6.3 earthquake (central Italy): New evidence from SBAS-DInSAR time series analysis. Geophys. Res. Lett. 37 (20) https://doi.org/10.1029/2010GL044780.
Lavecchia, G., Castaldo, R., De Nardis, R., De Novellis, V., Ferrarini, F., Pepe, S., Brozzetti, F., Solaro, G., Cirillo, D., Bonano, M., Boncio, P., Casu, F., De Luca, C., Lanari, R., Manunta, M., Manzo, M., Pepe, A., Zinno, I., Tizzani, P., 2016. Ground deformation and source geometry of the 24 August 2016 Amatrice earthquake (Central Italy) investigated through analytical and numerical modeling of DInSAR measurements and structural-geological data. Geophys. Res. Lett. 43 (24), 12–389. https://doi.org/10.1002/2016GL071723.
Li, Z., Feng, W., Xu, Z., Cross, P., Zhang, J., 2008. The 1998 Mw 5.7 Zhangbei Shangyi (China) earthquake revisited: a buried thrust fault revealed with interferometric synthetic aperture radar. Geochem. Geophys. Geosyst. 9 (4) https://doi.org/10.1029/2007GC001910.
Liberatore, D., Doglioni, C., Al Shawa, O., Atzori, S., Sorrentino, L., 2019. Effects of coseismic ground vertical motion on masonry constructions damage during the 2016 Amatrice-Norcia (Central Italy) earthquakes. Soil Dyn. Earthq. Eng. 120 (2019), 423–435. https://doi.org/10.1016/j.soildyn.2019.02.015.
Livio, F., Serva, L., Gürpinar, A., 2017. Locating distributed faulting: Contributions from InSAR imaging to probabilistic fault displacement hazard analysis (PFDHA). Quat. Int. 451, 223–233.
Luzi, L., Pacor, F., Puglia, R., 2017. Italian Accelerometric Archive v. 2.3. Istituto Nazionale di Geofisica e Vulcanologia, Dipartimento della Protezione Civile Nazionale. [WWW Document]. https://doi.org/10.13127/ITACA.2.3.
Mariani, M., Pugi, F., 2019. La Componente Sismica Verticale È Sempre da Considerare Perchè Rilevante Vicino e Lontano Dalla Sorgente. https://www.ingenio-web.it/25129-la-componente-sismica-verticale-e-sempre-da-considerare-perche-rilevante-vicino-e-lontano-dalla-sorgente.
Marotta, A., Sorrentino, L., Liberatore, D., Ingham, J.M., 2018. Seismic risk assessment of New Zealand unreinforced masonry churches using statistical procedures. Int. J. Archit. Herit. 12, 448–464. https://doi.org/10.1080/15583058.2017.1323242.
Martino, S., Prestininzi, A., Romeo, R.W., 2014. Earthquake-induced ground failures in Italy from a reviewed database. Nat. Hazards Earth Syst. Sci. 14 (4), 799.
Masi, A., Chiauzzi, L., Braga, F., Mucciarelli, M., Vona, M., Ditommaso, R., 2011. Peak and integral seismic parameters of L'Aquila 2009 ground motions: observed versus code provision values. Bull. Earthq. Eng. 9, 139–156. https://doi.org/10.1007/s10518-010-9227-1.
Massonnet, D., Rossi, M., Carmona, C., Adragna, F., Peltzer, G., Feigl, K., Rabaute, T., 1993. The displacement field of the Landers earthquake mapped by radar interferometry. Nature 364 (6433), 138–142.
Mele, G., Rovelli, A., Fodarella, A., Mancini, M., 2020. Site Effects of Onna during the 2009 L'Aquila (Central Italy) Seismic Sequence: Constraints on Bedrock Depth and 1D Local Velocity Structure from Aftershock Seismograms. Bull. Seismol. Soc. Am. 110 (2), 399–409.
Milana, G., Cultrera, G., Bordoni, P., Bucci, A., Cara, F., Cogliano, R., Di Giulio, G., Di Naccio, D., Famiani, D., Fodarella, A., Mercuri, A., 2019. Local site effects estimation at Amatrice (Central Italy) through seismological methods. Bull. Earthq. Eng. 18 (12), 5713–5739.
Monterroso, F., Bonano, M., Luca, C.D., Lanari, R., Manunta, M., Manzo, M., Onorato, G., Zinno, I., Casu, F., 2020. A global archive of coseismic DInSAR products obtained through unsupervised Sentinel-1 data processing. Rem. Sens. 12 (19), 3189. https://doi.org/10.3390/rs12193189.
Mouyiannou, A., Penna, A., Rota, M., Graziotti, F., Magenes, G., 2014. Implications of cumulative seismic damage on the seismic performance of unreinforced masonry buildings. Bull. N. Z. Soc. Earthq. Eng. 47, 157–170.
Neyman, J., Pearson, E.S., 1933. On the problem of the most efficient tests of statistical hypotheses. Philos. Trans. R. Soc. Lond. 231, 289–337.
Pedersen, R., Jónsson, S., Árnadóttir, T., Sigmundsson, F., Feigl, K.L., 2003. Fault slip distribution of two June 2000 MW6. 5 earthquakes in South Iceland estimated from joint inversion of InSAR and GPS measurements. Earth Planet. Sci. Lett. 213 (3–4), 487–502. https://doi.org/10.1016/S0012-821X(03)00302-9.
Petricca, P., Bignami, C., Doglioni, C., 2021. The epicentral fingerprint of earthquakes marks the coseismically activated volume. Earth Sci. Rev. 103667. https://doi.org/10.1016/j.earscirev.2021.103667.
Pezzo, G., Merryman Boncori, J.P., Tolomei, C., Salvi, S., Atzori, S., Antonioli, A., Trasatti, E., Novali, F., Serpelloni, E., Candela, L., Giuliani, R., 2013. Coseismic Deformation and Source Modeling of the May 2012 Emilia (Northern Italy) Earthquakes. Seismol. Res. Lett. 84 (4), 645–655. https://doi.org/10.1785/0220120171.
Ross, S.M., 2004. Introduction to Probability and Statistics for Engineers and Scientists. Elsevier Academic Press.
Rossi, A., Tertulliani, A., Azzaro, R., Graziani, L., Rovida, A., Maramai, A., Pessina, V., Hailemikael, S., Buffarini, G., Bernardini, F., Camassi, R., Del Mese, S., Ercolani, E., Fodarella, A., Locati, M., Martini, G., Paciello, A., Paolini, S., Arcoraci, L., Castellano, C., Verrubbi, V., Stucchi, M., 2019. The 2016-2017 earthquake sequence in Central Italy: macroseismic survey and damage scenario through the EMS-98 intensity assessment. Bull. Earthq. Eng. 17 (5), 2407–2431. https://doi.org/10.1007/s10518-019-00556-w.
Rovida, A., Locati, M., Camassi, R., Lolli, B., Gasperini, P., 2019. Catalogo Parametrico dei Terremoti Italiani (CPTI15), versione 2.0. Istituto Nazionale di Geofisica e Vulcanologia (INGV). doi:10.13127/CPTI/CPTI15.2.
Ruhl, C.J., Melgar, D., Geng, J., Goldberg, D.E., Crowell, B.W., Allen, R.M., Bock, Y., Barrientos, S., Riquelme, S., Baez, J.C., Cabral-Cano, E., 2019. A global database of strong-motion displacement GNSS recordings and an example application to PGD scaling. Seismol. Res. Lett. 90 (1), 271–279.
Salustri Galli, C., Torrini, A., Doglioni, C., Scrocca, D., 2002. Divide and highest mountains vs subduction in the Apennines. Studi Geol. Camerti 1, 143–153.
Salvi, S., Stramondo, S., Cocco, M., Tesauro, M., Hunstad, I., Anzidei, M., Briole, P., Baldi, P., Sansosti, E., Fornaro, G., Lanari, R., Doumaz, F., Pesci, A., Lanari, R., 2000. Modeling coseismic displacements resulting from SAR interferometry and GPS measurements during the 1997 Umbria-Marche seismic sequence. J. Seismol. 4 (4), 479–499. https://doi.org/10.1023/A:1026502803579.
Schiappapietra, E., Felicetta, C., D'Amico, M., 2021. Fling-step recovering from near-source waveforms database. Geosciences 11 (2), 67.
Sorrentino, L., Cattari, S., da Porto, F., Magenes, G., Penna, A., 2019. Seismic behaviour of ordinary masonry buildings during the 2016 Central Italy earthquakes. Bull. Earthq. Eng. 17, 5583–5607. https://doi.org/10.1007/s10518-018-0370-4.
Stafford, P.J., Berrill, J.B., Pettinga, J.R., 2009. New predictive equations for Arias intensity from crustal earthquakes in New Zealand. J. Seismol. 13, 31–52. https://doi.org/10.1007/s10950-008-9114-2.

Stramondo, S., Chini, M., Bignami, C., Salvi, S., Atzori, S., 2010. X-, C-, and L-band DInSAR investigation of the April 6, 2009, Abruzzi earthquake. IEEE Geosci. Remote Sens. Lett. 8 (1), 49–53. https://doi.org/10.1109/LGRS.2010.2051015.

Tertulliani, A., Arcoraci, L., Berardi, M., Bernardini, F., Brizuela, B., Castellano, C., Del Mese, S., Ercolani, E., Graziani, L., Maramai, A., Rossi, A., Sbarra, M., Vecchi, M., 2012. Emilia 2012 sequence: the macroseismic survey. In: "The Emilia (northern Italy) seismic sequence of May-June, 2012: preliminary data and results" edited by M. Anzidei, A. Maramai and P. Montone, 55. Ann. Geophys. 4, 2012. https://doi.org/10.4401/ag-6140.

Tizzani, P., Castaldo, R., Solaro, G., Pepe, S., Bonano, M., Casu, F., Manunta, M., Manzo, M., Pepe, A., Samsonov, S., Lanari, R., Sansosti, E., 2013. New insights into the 2012 Emilia (Italy) seismic sequence through advanced numerical modeling of ground deformation InSAR measurements. Geophys. Res. Lett. 40 (10), 1971–1977. https://doi.org/10.1002/grl.50290.

Trasatti, E., Kyriakopoulos, C., Chini, M., 2011. Finite element inversion of DInSAR data from the Mw 6.3 L'Aquila earthquake, 2009 (Italy). Geophys. Res. Lett. 38 (8) https://doi.org/10.1029/2011GL046714.

Trifunac, M.D., Brady, A.G., 1975. A study on the duration of strong earthquake ground motion. Bull. Seismol. Soc. Am. 65, 581–626. https://doi.org/10.1016/0148-9062(76)90487-3.

Trigila, A., Iadanza, C., 2008. Landslides in Italy, 83. Italian National Institute for Environmental Protection and Research (ISPRA). ISBN 88-488-0355-1.

Uang, C., Bertero, V., 1988. Implications of recorded earthquake ground motions on seismic design of building structures UCB/EERC- 88/13. In: Rep. n. UCB/EERC-88/13.

Valerio, E., Tizzani, P., Carminati, E., Doglioni, C., Pepe, S., Petricca, P., De Luca, C., Bignami, C., Solaro, G., Castaldo, R., De Novellis, V., Lanari, R., 2018. Ground deformation and source geometry of the 30 October 2016 Mw 6.5 Norcia earthquake (central Italy) investigated through seismological data, DInSAR measurements, and numerical modelling. Rem. Sens. 10 (12), 1901. https://doi.org/10.3390/rs10121901.

Valerio, E., Manzo, M., Casu, F., Convertito, V., De Luca, C., Manunta, M., Monterroso, F., Lanari, R., De Novellis, V., 2020. Seismogenic Source Model of the 2019, Mw 5.9, East-Azerbaijan Earthquake (NW Iran) through the Inversion of Sentinel-1 DInSAR Measurements. Rem. Sens. 12 (8), 1346. https://doi.org/10.3390/rs12081346.

Vanmaercke, M., Ardizzone, F., Rossi, M., Guzzetti, F., 2017. Exploring the effects of seismicity on landslides and catchment sediment yield: an Italian case study. Geomorphology 278, 171–183.

Wang, H., Xu, C., Ge, L., 2007. Coseismic deformation and slip distribution of the 1997 Mw7. 5 Manyi, Tibet, earthquake from InSAR measurements. J. Geodyn. 44 (3–5), 200–212. https://doi.org/10.1016/j.jog.2007.03.003.

Wang, X., Liu, G., Yu, B., Dai, K., Zhang, R., Chen, Q., Li, Z., 2014. 3D coseismic deformations and source parameters of the 2010 Yushu earthquake (China) inferred from DInSAR and multiple-aperture InSAR measurements. Rem. Sens. Envir. 152, 174–189. https://doi.org/10.1016/j.rse.2014.06.014.

Weston, J., Ferreira, A.M., Funning, G.J., 2012. Systematic comparisons of earthquake source models determined using InSAR and seismic data. Tectonophysics 532, 61–81. https://doi.org/10.1016/j.tecto.2012.02.001.

Wilkinson, M.W., McCaffrey, K.J., Jones, R.R., Roberts, G.P., Holdsworth, R.E., Gregory, L.C., Walters, R.J., Wedmore, L., Goodall, H., Iezzi, F., 2017. Near-field fault slip of the 2016 Vettore Mw 6.6 earthquake (Central Italy) measured using low-cost GNSS. Sci. Rep. 7 (1), 1–7.

Wilks, S.S., 1938. The large sample distribution of the likelihood ratio for testing composite hypotheses. Ann. Math. Stat. 9, 60–62.

Wright, T.J., Lu, Z., Wicks, C., 2003. Source model for the Mw 6.7, 23 October 2002, Nenana Mountain earthquake (Alaska) from InSAR. Geophys. Res. Lett. 30 (18), 1974. https://doi.org/10.1029/2003GL018014.